Self-centering steel column base with metallic energy dissipation devices

Vasileios C. Kamperidis[a1*], Theodore L. Karavasilis[b2] and George Vasdravellis[c3]

[a] *School of Engineering, University of Warwick, Coventry, CV4 7AL, United Kingdom*

[b] *Faculty of Engineering and the Environment, University of Southampton, Highfield Southampton, SO17 1BJ, United Kingdom*

[c] *Institute for Infrastructure and Environment, Heriot-Watt University, Edinburgh, EH14 4AS, United Kingdom*

ABSTRACT

Column bases of seismic-resistant steel frames are typically designed as full-strength to ensure that plastic hinges develop in the bottom end of the first-storey columns. Alternatively, column bases may be designed as partial-strength and dissipate energy through inelastic deformations in their main components (i.e., base plate, steel anchor rods). Both design philosophies result in difficult-to-repair damage and residual drifts. Moreover, the second design philosophy results in complex hysteretic behaviour with strength and stiffness deterioration. This paper proposes a partial-strength low-damage self-centering steel column base. The column base provides flexibility in the design as its rotational stiffness and moment resistance can be independently tuned. The paper presents an analytical model that predicts the stiffness, strength, and hysteretic behaviour of the column base. In addition, a design procedure and detailed finite element models are presented. The paper evaluates the effectiveness of the column base by carrying out nonlinear dynamic analyses on a prototype steel building designed as post-tensioned self-centering moment-resisting frame. The results demonstrate the potential of the column base to reduce the residual first-storey drifts and protect the first-storey columns from yielding.

Keywords: column base; self-centering; low-damage; post-tensioned; seismic resilience; rocking.

[1*] Corresponding author, Ph.D., E-mail: V.Kamperidis@warwick.ac.uk, ORCID ID number: 0000-0003-4893-7110

[2] Professor of Structures and Structural Mechanics, E-mail: T.Karavasilis@soton.ac.uk

[3] Assistant Professor, E-mail: g.vasdravellis@hw.ac.uk

1 Introduction

Column bases are fundamental components of a seismic-resistant steel frame. Their rotational stiffness and moment resistance affect the storey drifts, the forces in the structural members, and the collapse resistance of a steel building [1–5]. Within the capacity design philosophy of EC8 [6], column bases are typically designed as full-strength joints [7] to ensure the formation of a plastic hinge within the bottom end of the column rather than in the column base [6]. Alternatively, column bases may be designed as partial-strength joints and dissipate energy through inelastic deformations in their main components (i.e., base plate, anchor rods). Both design philosophies result in difficult-to-repair damage and residual drifts. Moreover, the second design philosophy results in complex hysteretic behaviour with strength and stiffness deterioration. In terms of their rotational stiffness, column bases are in practice modelled as rigid or pinned, which rely on assumptions that do not accurately represent their actual behaviour. Such assumptions may either underestimate or overestimate the storey drifts and internal member forces, thus leading to designs that may be uneconomical or unsafe [2,3,5].

A number of research efforts exist on the development of column bases with self-centering and low-damage characteristics. Among the proposed column bases [4,8–18], a promising class are the post-tensioned (PT) column bases with energy dissipating devices. These column bases use PT tendons to clamp the column to the foundation and provide self-centering capability, and devices to dissipate seismic energy along with offering supplemental stiffness and strength. Previous studies on PT column bases demonstrated their ability to reduce residual storey drifts [4,14,17,19]. Ikenaga et al. [17,20] proposed a PT column base with yielding devices, which achieved self-centering capability under a certain level of rotation. However, the self-centering capability of the column base was restricted by the applicable length and plan view arrangement of the PT bars, which were placed within the perimeter of their wide flange column foot section. Under large rotations, tests showed residual rotations in the column base. Chou and Chen [4]

proposed a PT column base equipped with reduced flange plates used as yielding devices. PT bars, running along the length of the steel-concrete composite columns, were used to provide self-centering capability to the column bases. Their analyses showed that both the frame and PT column bases had small residual drifts under both the design and maximum considered earthquakes. Moreover, test results showed that post-tensioning the whole columns resulted in undesirable column axial shortening [21]. Chi and Liu [14] proposed a column base, which had conceptual similarities with the column base of Ikenaga et al. [17,20], but with longer tendons. Thus, their column base could achieve self-centering behaviour under larger rotations. However, the column base could not avoid loss of post-tensioning due to the large PT forces applied to the column foot. Tests also showed that some parts of the column base experienced undesirable plastic deformations. Recently, Chen et al. [18] proposed a self-centering column base with friction devices. Their column base achieved self-centering behaviour for large rotations. Yet, the column base could not avoid column axial shortening and worked only with open column sections.

This paper presents a partial-strength low-damage self-centering steel column base that uses PT tendons to achieve self-centering behaviour and hourglass shape steel yielding devices, referred to as web hourglass pins (WHPs) [22], to dissipate seismic energy. The WHPs are installed in a way that makes their post-earthquake replacement straightforward. The rotational stiffness and moment resistance of the column base can be independently tuned. Self-centering behaviour can be ensured even under very large base rotations by adjusting the position and characteristics of the tendons and WHPs. The PT tendons are anchored on the top of a strong column foot. The column foot receives the large PT forces instead of the column, increasing the rotation capacity of the latter and avoiding column axial shortening and loss of post-tensioning. Anchoring the PT tendons on the column foot avoids difficulties in structural detailing (i.e., congestion of structural components) at the first-storey beam-column connection. The column

base can work both with open steel as well as with steel and steel-concrete composite tubular sections and can dissipate seismic energy in both the strong and weak axis of the column. Lately, based on preliminary findings presented in [23], Freddi et al. [24] proposed a column base similar to the one proposed herein, but with friction EDs, a different mechanism to resist base shear, and a different column foot. The following sections present an analytical model that predicts the strength, stiffness and hysteretic behaviour of the PT column base with WHPs, a design procedure that sizes all its components for a target column base rotation, and nonlinear finite element method (FEM) models in the software Abaqus [25] and software OpenSees [26]. The latter model is used in the assessment of a steel building using the column base.

2 Description of the proposed column base

2.1 Structural details and concept development

Fig. 1 shows a three-dimensional representation of the upper part of the column base, while Fig. 2 shows drawings of its whole configuration that consists of four high-strength tendons and eight WHPs (four pairs).

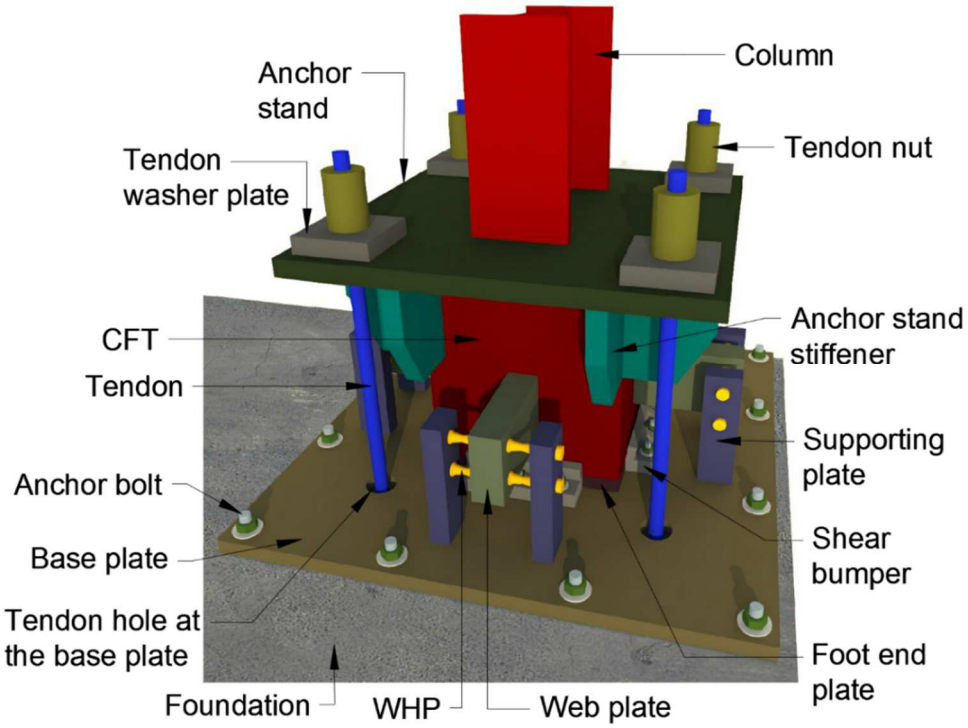

Fig. 1 Three-dimensional representation of the column base

The column is welded on an elevated strong steel plate, or anchor stand, which is, in turn, welded on a concrete filled steel tube (CFT) that serves as the column foot. The tendons are anchored on the anchor stand (Detail 1 of Fig. 2(a)) and to the bottom of the concrete foundation, running unbonded through steel ducts (Fig. 2(a)). The tendons are post-tensioned and clamp the CFT to a base plate, providing rotational stiffness, moment resistance and self-centering capability. Concepts with unbonded PT tendons were also used in the past in PT concrete [27–29] and PT steel-concrete composite columns [4,30,31]. In the aforementioned research, the tendons were running along the whole height of their host elements, loading them with their large PT forces. On the contrary, the tendons on the proposed column base are placed within the concrete foundation and exert their PT forces only on the CFT. As such, the CFT resists the PT forces instead of the column and thus the latter can avoid the undesirable axial shortening associated with the increased axial loading from the PT forces, as it was showed in [21]. According to Garlock et al. [32], preventing the axial shortening of a member associated with a PT connection can protect the tendons of the connection from loss of their post-tensioning force. As it is shown next in this research (Section 3.3), this finding can be extended in the proposed column base. Furthermore, avoiding to receive the large PT forces, the column achieves an increased rotation capacity [33]. Using the CFT as a column foot helps the column base to form a strong rocking interface and thus enhance its self-centering and low-damage attributes [34].

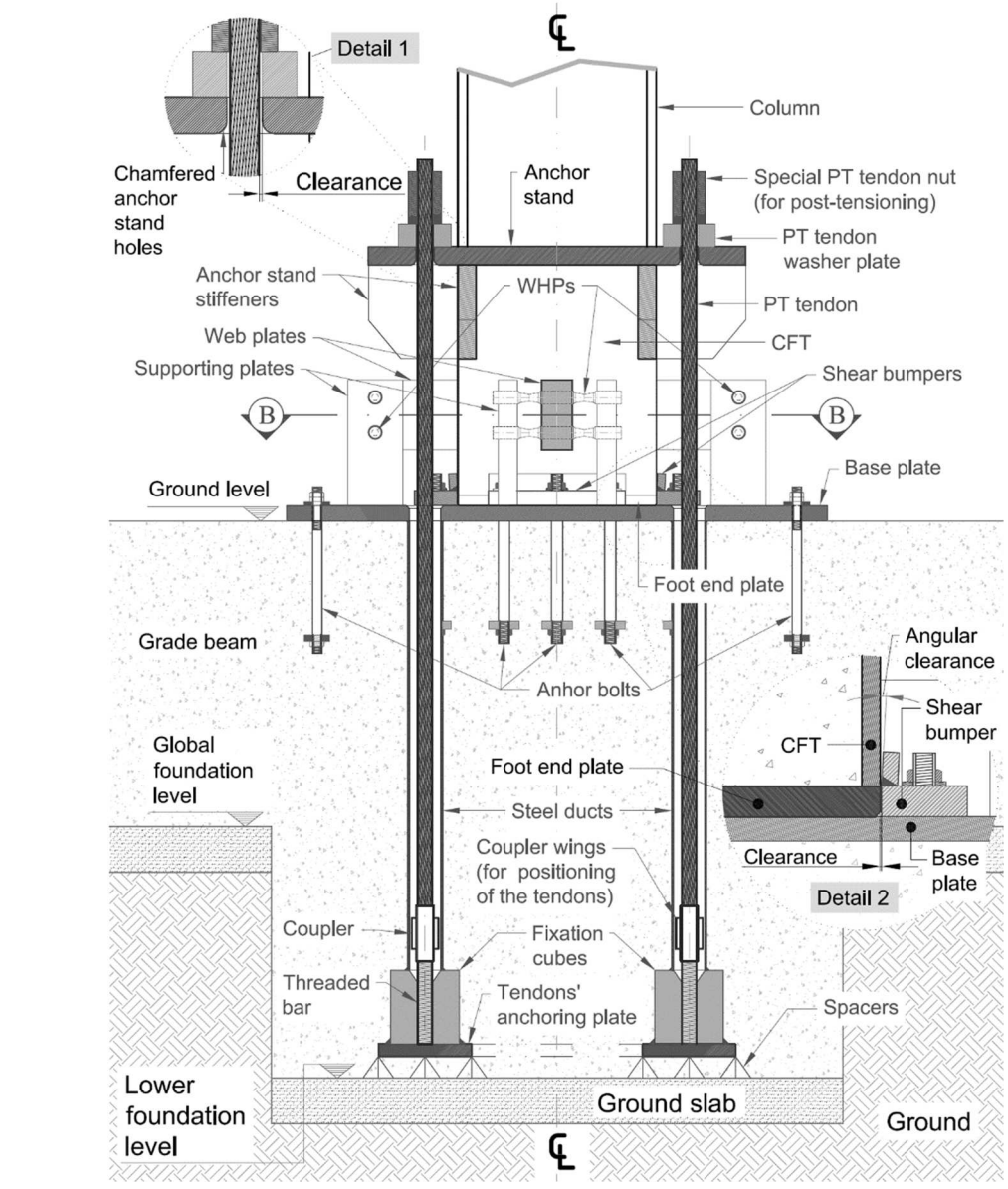

(a)

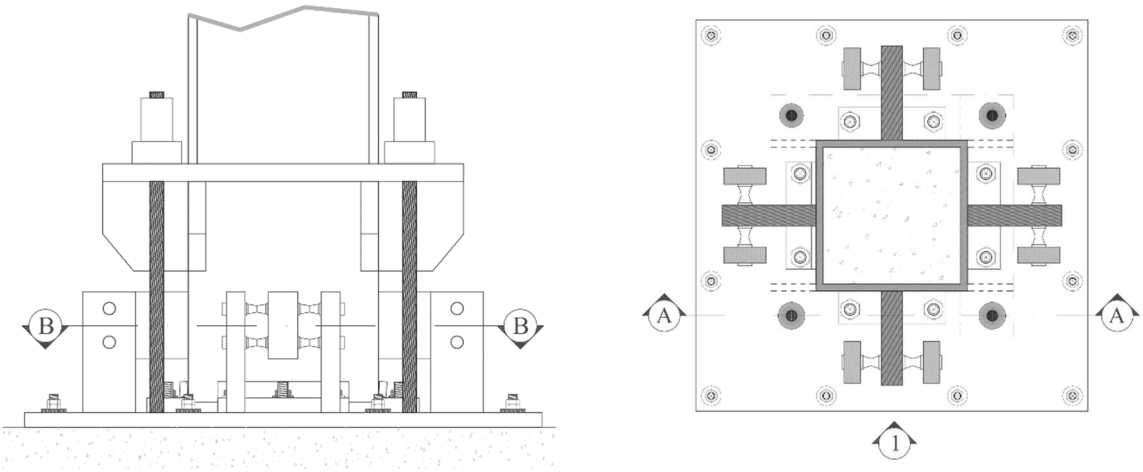

(b) **(c)**

Fig. 2 Drawings of the column base: (a) Vertical cross-section A-A; (b) Elevation 1; (c) Horizontal cross-section B-B

The anchor stand offers flexibility in the arrangement of the tendons, and thus, in the selection of their lever arms; the latter are defined as the horizontal distances of the tendons from the centre of rotation (COR) of the column base (Fig. 4). Therefore, the column base can control its stiffness and strength over its two axes. The anchor stand is reinforced with stiffeners to avoid excessive bending due to the large PT forces, protecting the tendons from loss of post-tensioning. The WHPs are inserted in aligned holes drilled on vertical plates, named supporting plates, and on horizontal plates, named web plates. The supporting plates are welded on the base plate, while the web plates on the four sides of the CFT (Fig. 1). The WHPs possess high fracture capacity due to their optimized shape (Fig. 3(a)) and provide repeatable and consistent energy dissipation through inelastic bending [35]. Except for the WHPs, the column base solely uses steel plated elements to avoid additional fabrication and machinery costs.

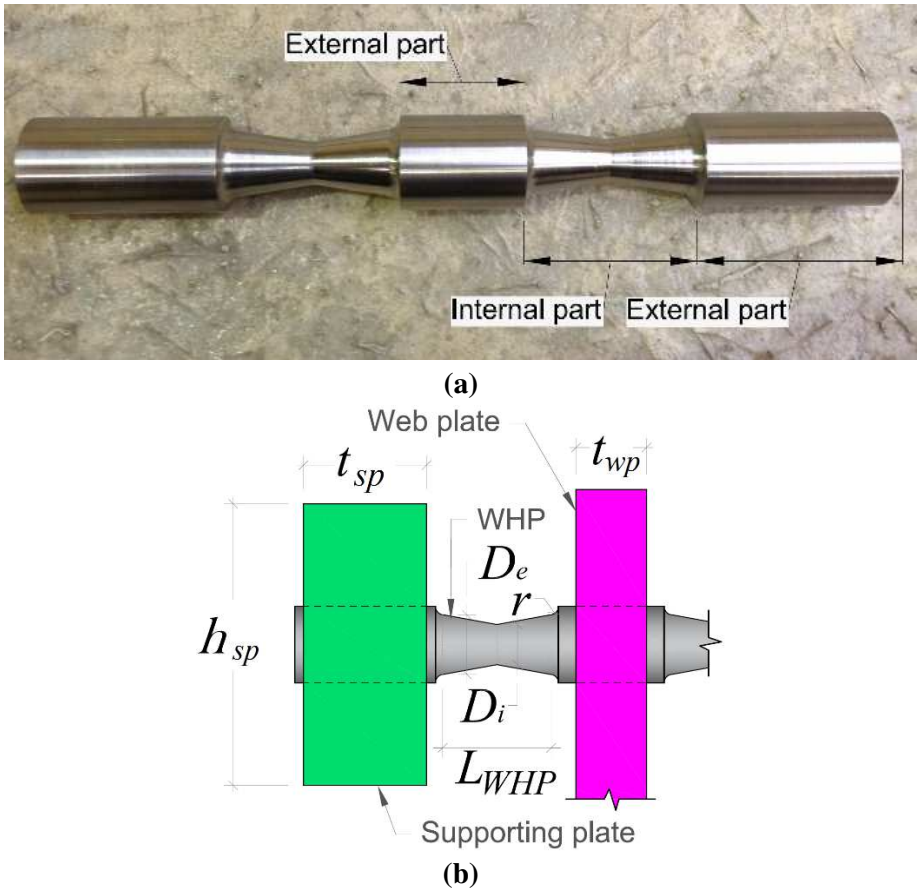

Fig. 3 (a) Photo of a single WHP; (b) notation and geometry of the supporting plate-web plate-WHP system (plan view)

Shear is resisted through friction in the rocking interface and through steel elements bolted on the base plate against the four sides of the CFT, named shear bumpers (Detail 2 in Fig. 2(a)). The shear bumpers are detailed to avoid interlocking during the CFT rocking. The proposed column base can resist seismic loading and dissipate seismic energy in both loading axes by appropriately selecting the lever arms and characteristics of the PT tendons and WHPs. However, this research investigates the case of uniaxial seismic loading.

2.2 Moment-rotation behaviour

Fig. 4 shows a free-body diagram of the proposed column base in the case of loading from left to right. Before the load is applied, the initial PT force in each tendon is equal to T. When the load initiates, the column base starts rocking about the COR. The rocking of the column base is quantified through the base rotation θ, which is defined as the angle developed between the base plate and the foot end plate (Fig. 1) of the CFT, as it can be seen in Fig 4.

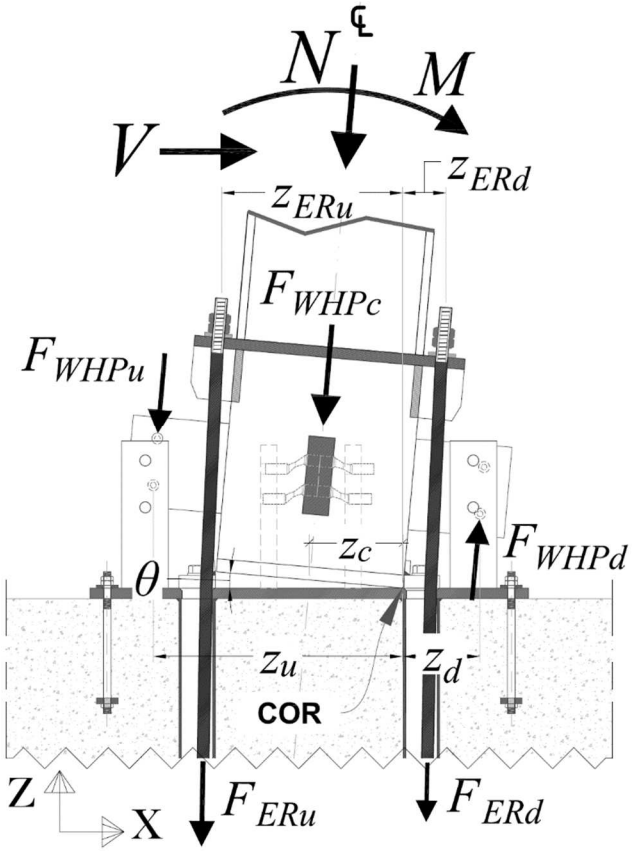

Fig. 4 Free-body diagram of the column base for lateral loading acting from left to right (F_{ERd} is eliminated in Case 2, after θ exceeds $\theta_{ERd,PTF}$)

The COR is assumed to be at the rocking toe (right leaning edge in Fig. 4) of the foot end plate. The rocking of the column base causes the left side of the anchor stand to move upwards (gap-opening side), elongating the left tendons, and the right side to move downwards (rocking-toe side), reducing the initial PT force in the right tendons. However, the latter tendons do not buckle because they lack underside nuts and avoid contact with the appropriately detailed oversized anchor stand holes, as it can be seen in Detail 1 of Fig. 2(a). The total force in the tendons at the gap-opening side is denoted as F_{ERu} and at the rocking-toe side as F_{ERd}. The lever arms of the forces F_{ERu} and F_{ERd} are z_{ERu} and z_{ERd}, respectively (Fig. 4).

Rocking of the column base causes also the WHPs to deform and develop forces. In Fig. 4, the force developed in the WHPs at the gap-opening side is denoted as F_{WHPu}, the force in the central WHPs (centreline of the column) as F_{WHPc}, and the force in the WHPs at the rocking-toe side as F_{WHPd}. The lever arms of these forces with respect to the COR are denoted as z_u, z_c, and z_d, respectively. The latter distances are defined as the horizontal distances between the COR and the geometric centre of each of the above three WHP groups.

N, M and V are the internal axial force, bending moment and shear force at the bottom of the column. The total moment resistance of the column base, M, is given by:

$$M = M_N + M_{WHP} + M_{ER} \tag{1}$$

where M_N, M_{WHP}, and M_{ER} are the moment contributions of N, WHPs, and tendons, respectively.

Two behaviour cases are identified. In the first case, referred to as Case 1, the tendons at the rocking-toe side do not lose their post-tensioning up to the target base rotation, θ_t, and thus the forces in the column base are those of Fig. 4. In the second case, referred to as Case 2, complete loss of post-tensioning takes place before θ_t is reached. The complete loss of post-tensioning in the tendons at the rocking-toe side is represented by the base rotation $\theta_{ERd,PTF}$, described in Step

2 of the design procedure presented below (Section 2.3). After $\theta_{ERd,PTF}$ is reached, F_{ERd} in Fig. 4 is eliminated. Based on the above, Case 1 is expressed as $\theta_t < \theta_{ERd,PTF}$ and Case 2 as $\theta_{ERd,PTF} < \theta_t$. In both cases, for the column base to achieve a self-centering behaviour up to θ_t, the tendons must avoid yielding under latter rotation. This concept was also used by previous research in PT column bases with energy dissipation devices [4,14,18]. To avoid yielding, the tendons are designed according to Step 2 of the design procedure in Section 2.3.

Case 1

Fig. 5(a) shows the theoretical cyclic moment-base rotation (M-θ) behaviour of the column base for Case 1. After decompression (Point 1 in Fig. 5(a)), gap opens and the behaviour of the column base becomes nonlinear elastic with rotational stiffness S_{12}.

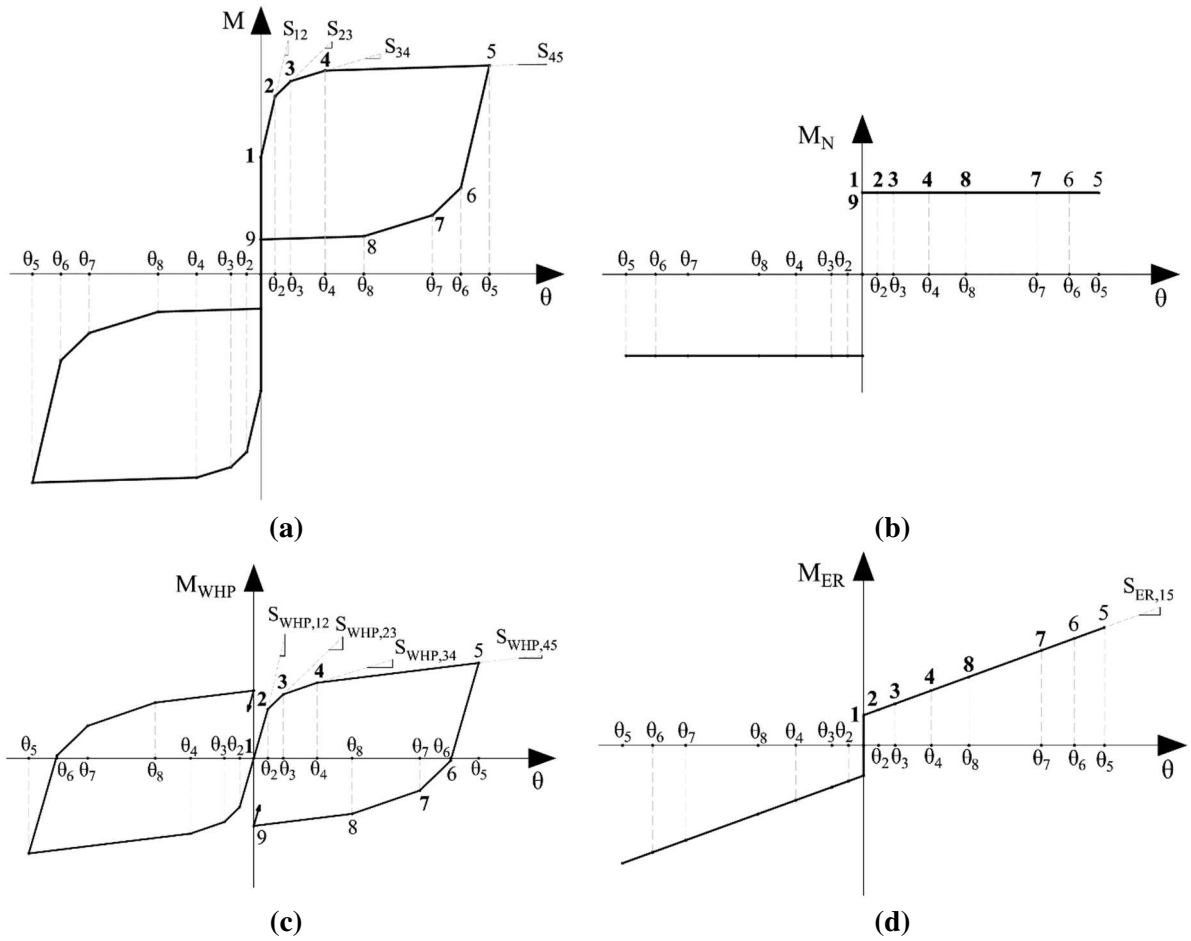

Fig. 5 (a) Theoretical cyclic M-θ behaviour of the column base in Case 1; (b) moment contribution of N; (c) moment contribution of the WHPs; (d) moment contribution of the PT tendons

At Point 2, the WHPs at the gap-opening side yield and M continues to increase with slope S_{23}. At Point 3, the central WHPs yield and M continues to increase with slope S_{34}. At point 4, the WHPs at the rocking-toe side yield and M continues to increase with slope S_{45} up to Point 5, corresponding to θ_t which is represented by rotation θ_5. Upon loading reversal, the column base begins to unload until the gap closes. Equations to calculate S_{12}, S_{23}, S_{34}, S_{45}, θ_2, θ_3, θ_4, and θ_5 are provided in Section 2.3, while equations for θ_6, θ_7, and θ_8, in Section 2.4. $S_{WHP,12}$, $S_{WHP,23}$, $S_{WHP,34}$ and $S_{WHP,45}$ are the values of the rotational stiffness in the respective branches of the M_{WHP}-θ diagram (Fig. 5(c)), while $S_{ER,15}$ is the rotational stiffness of the M_{ER}-θ diagram (Fig. 5(d)).

The M_{WHP}-θ behaviour is considered multi-linear elastoplastic. When loading is reversed, all the WHPs and tendons at the gap-opening side unload with their elastic stiffness up to Point 6, while each tendon at the rocking-toe side recovers a part of its initial post-tensioning with its elastic stiffness, K_{ER} (defined in Step 2 of Section 2.3). The tendons at the gap-opening side continue to unload with the same K_{ER} until the gap closes, where they finally recover their initial post-tensioning since they do not yield. Post-tensioning in the tendons at the rocking-toe side continues to increase until it is fully recovered at gap closing. From Point 6 to 7, each WHP at the gap-opening side unloads with its post-elastic stiffness, K_{fp}, while the central and the WHPs at the rocking-toe side unload with their elastic stiffness, K_{fe}. From Point 7 to 8, both the central and the WHPs at the gap-opening side unload with K_{fp}, while only the WHPs at the rocking-toe side continue to unload with K_{fe}. From Point 8 to 9, all WHPs unload with K_{fp}. Due to the small values of θ, M_N is assumed to be of constant magnitude (Fig. 5(b)) and no negative stiffness is considered due to rocking [36]. K_{fe} and K_{fp} are defined in Step 3 and 4 of Section 2.3, respectively.

Case 2

Fig. 6(a) shows the theoretical cyclic M-θ behaviour of the column base in Case 2. Case 2 follows the same procedure with Case 1 up to Point 5, where the tendons at the rocking-toe side

lose their post-tensioning. From Point 5 to 6, M continues to increase with slope S_{56} (Eq. (18) below), with the tendons at the rocking-toe side no longer contributing to moment resistance since they lose contact with the anchor stand. Point 6 corresponds to θ_t and is represented by θ_6 (Section 2.4.2). Upon loading reversal, the column base begins to unload until the gap closes.

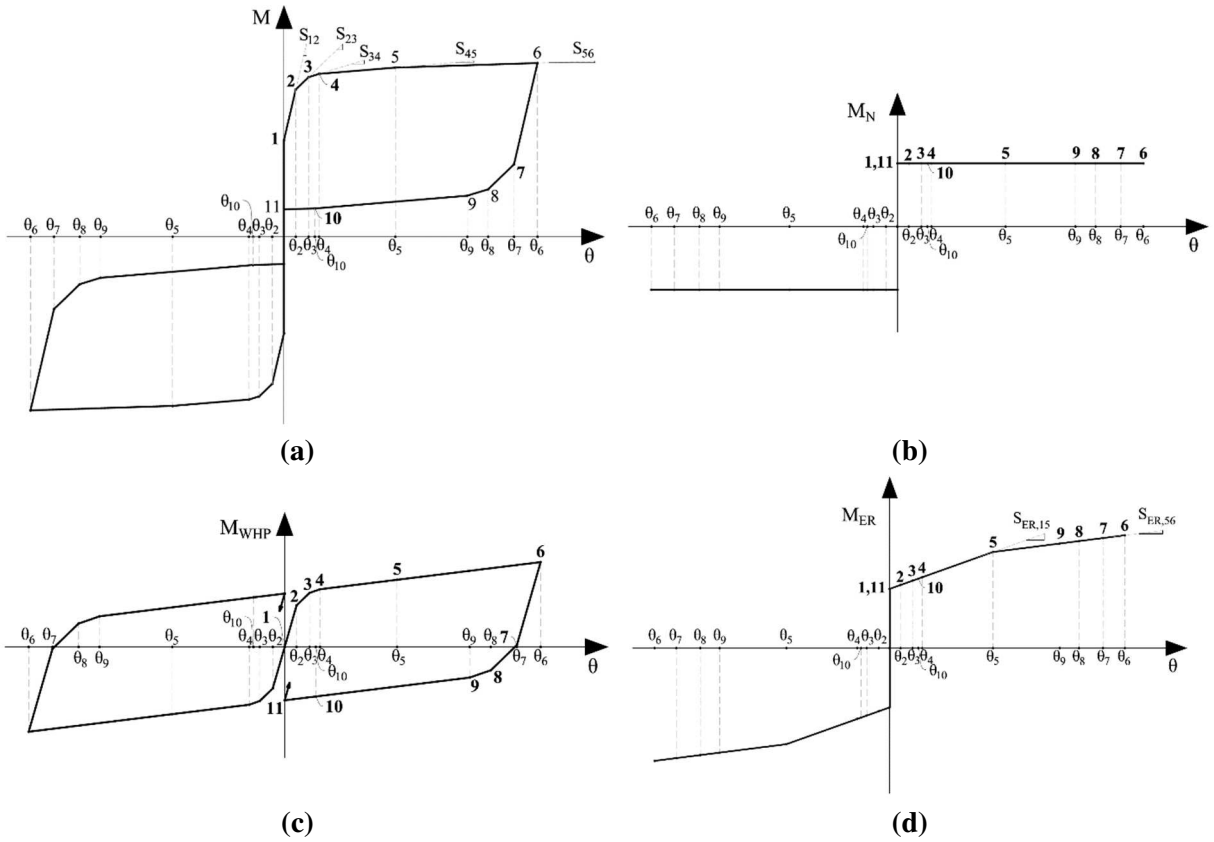

Fig. 6 (a) Theoretical cyclic M-θ behaviour of the proposed column base in Case 2; (b) moment contribution of N; (c) moment contribution of the WHPs; (d) moment contribution of the PT tendons

The M_{WHP}-θ behaviour is considered multi-linear elastoplastic. When loading is reversed, all the WHPs and tendons at the gap-opening side unload with their elastic stiffness up to Point 7, while the tendons at the rocking-toe side are PT-free and will remain as such up to Point 10. From Point 7 to 8, the WHPs and tendons at the gap-opening side continue to unload with their elastic stiffness. The latter tendons continue to unload with K_{ER} until the gap closes. From Point 8 to 9, the WHPs at the gap-opening side unload with K_{fp}, while the central and the WHPs at rocking-toe side unload with K_{fe}. From Point 9 to 10, both the central and the WHPs at the gap-opening side unload with K_{fp}, while the WHPs at the rocking-toe side continue to unload with

K_{fe}. From Point 10 to 11, all WHPs unload with K_{fe} and the tendons at the rocking-toe side start recovering their initial post-tensioning with K_{ER} up to Point 11, where the gap closes.

2.3 Design procedure

The proposed design procedure of the column base is a step-by-step performance-based design approach that ensures a low-damage and self-centering behaviour, sizes its main components (i.e., the tendons, WHPs, web and supporting plates of the WHPs, and CFT), and tunes the strength and stiffness of the column base.

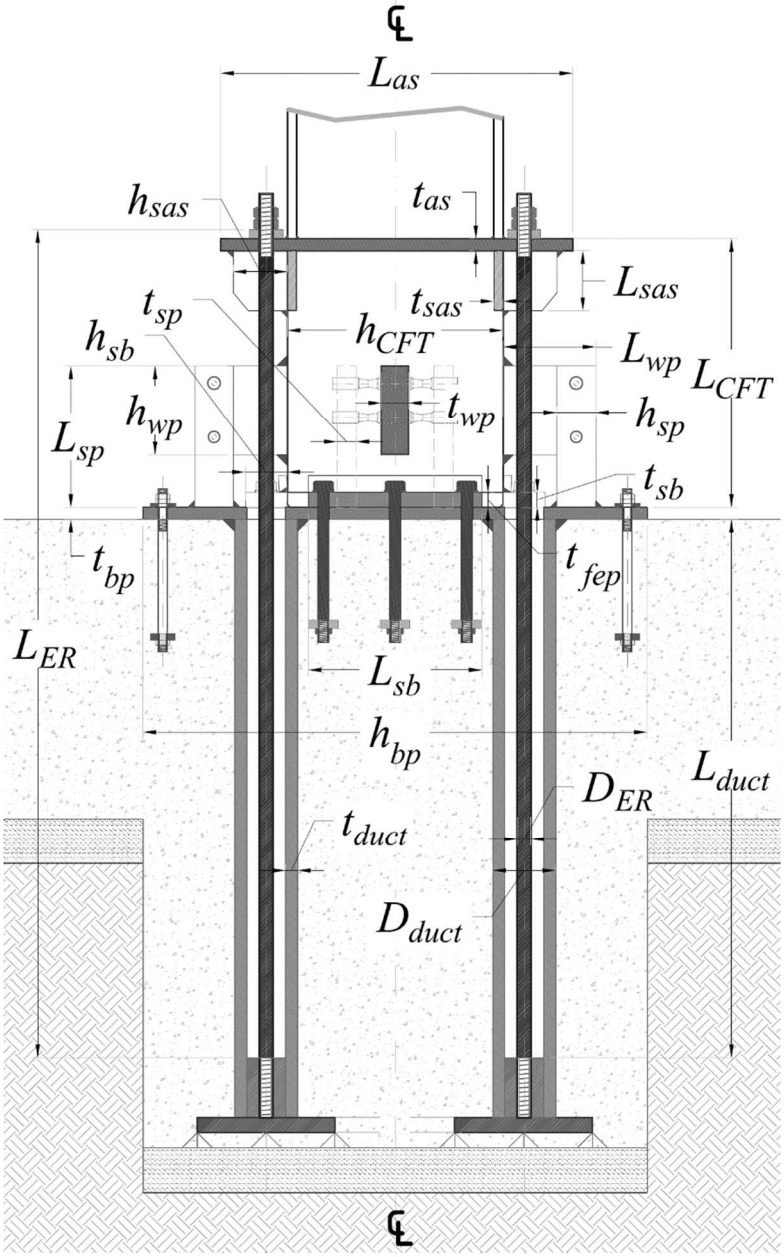

Fig. 7 Notation for the column base (explained in Table 1)

The minimum height of the CFT, L_{CFT} (Fig. 7), is selected to provide adequate space so that all the components between the base plate and anchor stand (the design of which will be determined in the following paragraphs) be accommodated. Considering the latter, one can select an appropriate L_{CFT} and thus determine a target initial stiffness of a first-storey column as being equal to that of a fully fixed column with height equal to that of the first storey minus L_{CFT}. The rest of the components of the column base (e.g., the anchor stand, anchor stand stiffeners, etc.) are designed to European standards [7,37–40] in order to have appropriate dimensions and, so, to remain elastic (and thus damage-free) under the stresses that are expected to develop. The design procedure takes as input the column section and column axial force, N. Similar to previous research on PT column bases [4,41], N is assumed equal to the axial force calculated from analysis for the gravity loads of the seismic design combination, i.e., $N_{Ed,G}$ per EC8. The design procedure includes the following steps:

Step 1: Calculation of the initial post-tensioning force

Select a value for the ratio $M_{IGO}/M_{N,pl,Rd,c}$, where M_{IGO} is the moment at Point 2 in both Cases 1 (Fig. 5(a)) and 2 (Fig. 6(a)), and $M_{N,pl,Rd,c}$ is the plastic moment resistance of the column, appropriately reduced to account for the interaction with the maximum axial force anticipated in the column, so that premature column yielding is avoided [6]. The aforementioned ratio should be less than one for the moment resistance of the column base to be lower than that of the column, protecting thus the latter from yielding. By appropriately modifying the $M_{IGO}/M_{N,pl,Rd,c}$ ratio, the strength of the column base can be tuned. Then, select a value for the ratio M_D/M_{IGO} and calculate the moment M_D. M_D is the moment at the onset of rocking and corresponds to Point 1 for both Case 1 and 2. In past research [42,43], M_D is referred as decompression moment because it is the moment at which the gap opens. According to [44], M_D/M_{IGO} should be larger than 0.5 to

approximately achieve self-centering behaviour. The initial post-tensioning force at each tendon, T, is given by the relation:

$$T = \frac{M_D - 0.5 \cdot N \cdot h_{CFT}}{n_{ERu} \cdot z_{ERu} - n_{ERd} \cdot z_{ERd}} \tag{2}$$

where n_{ERu} and n_{ERd} is the number of the tendons at the gap-opening and rocking-toe side, respectively, and h_{CFT} is the cross-sectional depth of the CFT, described in Fig. 7.

Step 2: Design the tendons

Select a yield strength, $f_{y,ER}$, and assume a diameter, D_{ER}, for the PT tendons. To avoid yielding for θ_t, the tendons must have a minimum length, L_{ER}, which is given by the following relationship:

$$L_{ER} \geq \frac{E_{ER} \cdot A_{ER} \cdot z_{ERu} \cdot \theta_t}{f_{y,ER} \cdot A_{ER} - T} \tag{3}$$

where E_{ER} is the modulus of elasticity of the tendons and A_{ER} is each tendon's cross-sectional area. Relationship (3) is the check for the yielding of the PT tendons; for a given L_{ER} and keeping all the other parameters constant, one can turn the aforementioned relationship into an equality and solve for the base rotation at which the PT tendons yield. Once L_{ER} is defined, $\theta_{ERd,PTF}$ can be determined as follows:

$$\theta_{ERd,PTF} = \frac{T}{K_{ER} \cdot z_{ERd}} \tag{4}$$

where $K_{ER}=E_{ER} \cdot A_{ER}/L_{ER}$. Depending on the $\theta_{ERd,PTF}$ value, Case 1 or 2 is concluded (Section 2.2).

Step 3: Design the WHPs

Select the number of the WHPs at the gap-opening and rocking-toe side, and that of the central WHPs, denoted as n_{WHPu}, n_{WHPd} and n_{WHPc}, respectively. Then estimate the yield strength of each WHP, $F_{y,WHP,i}$, according to the following relationship:

$$F_{y,WHP,i} = \frac{z_u \cdot \left[M_{IGO} - 0.5 \cdot N \cdot h_{CFT} - M_{ER}(\theta_2) \right]}{n_{WHPu} \cdot z_u^2 + n_{WHPc} \cdot z_c^2 + n_{WHPd} \cdot z_d^2} \tag{5}$$

where $M_{ER}(\theta_2)$ is the moment contribution of all PT tendons for θ_2. $M_{ER}(\theta_2)$ is given by the relationship:

$$M_{ER}\left(\theta_2\right) = K_{ER} \cdot \left(n_{ERu} \cdot z_{ERu}^2 + n_{ERd} \cdot z_{ERd}^2 \right) \cdot \theta_2 + \left(n_{ERu} \cdot z_{ERu} - n_{ERd} \cdot z_{ERd} \right) \cdot T \tag{6}$$

Assuming that the moment contribution of the rocking to M_{ER} is negligible at Point 2, M_{ER} is considered constant between Points 1 and 2 for both Case 1 and 2. Hence:

$$M_{ER}\left(\theta_2\right) \cong \left(n_{ERu} \cdot z_{ERu} - n_{ERd} \cdot z_{ERd} \right) \cdot T \tag{7}$$

Substituting M_{ER} from Eq. (7) into Eq. (5), a first estimate of $F_{y,WHP,i}$ is obtained. First estimates for θ_2, θ_3 and θ_4 can then be derived by the relationships:

$$\theta_2 = \frac{F_{y,WHP,i}}{K_{fe} \cdot z_u}; \quad \theta_3 = \frac{F_{y,WHP,i}}{K_{fe} \cdot z_c}; \quad \theta_4 = \frac{F_{y,WHP,i}}{K_{fe} \cdot z_d} \tag{8}$$

where K_{fe} is derived from [22]. The estimated value of θ_2 is then used in Eq. (6) to give a better estimation of $M_{ER}(\theta_2)$. $M_{ER}(\theta_2)$ is then substituted in Eq. (5) to provide a new $F_{y,WHP,i}$ and the WHP design procedure is repeated. The external (D_e) and internal (D_i) diameters of the WHPs (Fig. 3(b)) can be calculated by substituting the final $F_{y,WHP,i}$ in the equations provided in [22,45]. The clear length of the bending parts of half a WHP, L_{WHP}, also described in Fig. 3(b), is defined according to [22]. The web and supporting plates are then designed according to [35].

Step 4: Self-centering capability

The self-centering capability of the column base is examined separately for Case 1 and 2.

Case 1

In Case 1, the following criteria must be met:

$$M_D \geq (S_{12} - S_{23}) \cdot \theta_2 \quad for \quad \theta_2 \leq \theta_t < \theta_3 \tag{9}$$

$$M_D \geq (S_{12} - S_{23}) \cdot \theta_2 + (S_{23} - S_{34}) \cdot \theta_3 \quad for \quad \theta_3 \leq \theta_t < \theta_4 \tag{10}$$

$$M_D \geq (S_{12} - S_{23}) \cdot \theta_2 + (S_{23} - S_{34}) \cdot \theta_3 + (S_{34} - S_{45}) \cdot \theta_4 \quad for\, \theta_4 \leq \theta_t \leq \theta_5 \tag{11}$$

If Relations (9), (10), or (11) are not satisfied, return to Step 1 and repeat the design procedure with a higher M_D/M_{IGO} ratio.

In the above relations, the rotational stiffness for each of the branches of the hysteretic loop of Fig. 5(a) are defined as follows:

S_{12} for Points 1-2 ($\theta_1 < \theta \leq \theta_2$):

$$S_{12} = K_{fe} \cdot \left(n_{WHPu} \cdot z_u^2 + n_{WHPc} \cdot z_c^2 + n_{WHPd} \cdot z_d^2 \right) + K_{ER} \cdot \left(n_{ERu} \cdot z_{ERu}^2 + n_{ERd} \cdot z_{ERd}^2 \right) \tag{12}$$

S_{23} for Points 2-3 ($\theta_2 < \theta \leq \theta_3$):

$$S_{23} = K_{fe} \cdot \left(\lambda \cdot n_{WHPu} \cdot z_u^2 + n_{WHPc} \cdot z_c^2 + n_{WHPd} \cdot z_d^2 \right) + K_{ER} \cdot \left(n_{ERu} \cdot z_{ERu}^2 + n_{ERd} \cdot z_{ERd}^2 \right) \tag{13}$$

S_{34} for Points 3-4 ($\theta_3 < \theta \leq \theta_4$):

$$S_{34} = K_{fe} \cdot \left(\lambda \cdot n_{WHPu} \cdot z_u^2 + \lambda \cdot n_{WHPc} \cdot z_c^2 + n_{WHPd} \cdot z_d^2 \right) + K_{ER} \cdot \left(n_{ERu} \cdot z_{ERu}^2 + n_{ERd} \cdot z_{ERd}^2 \right) \tag{14}$$

S_{45} for Points 4-5 ($\theta_4 < \theta \leq \theta_5$):

$$S_{45} = K_{fe} \cdot \left(\lambda \cdot n_{WHPu} \cdot z_u^2 + \lambda \cdot n_{WHPc} \cdot z_c^2 + \lambda \cdot n_{WHPd} \cdot z_d^2 \right) + K_{ER} \cdot \left(n_{ERu} \cdot z_{ERu}^2 + n_{ERd} \cdot z_{ERd}^2 \right) \tag{15}$$

where the factor λ is the K_{fp}/K_{fe} ratio, equal to 2% according to [22]. The rotational stiffness for each of the unloading parts of the first half hysteretic loop can be derived as follows:

$$S_{56} = S_{12}; \quad S_{67} = S_{23}; \quad S_{78} = S_{34}; \quad S_{89} = S_{45} \tag{16}$$

Case 2

In Case 2, Relations (9) and (10) remain in effect. For $\theta_4 \le \theta_t < \theta_5$ ($\theta_5 = \theta_{ERd,PTF}$), M_D is checked against Relation (11). For $\theta_5 \le \theta_t \le \theta_6$, the following criterion must be met:

$$M_D \ge (S_{12} - S_{23}) \cdot \theta_2 + (S_{23} - S_{34}) \cdot \theta_3 + (S_{34} - S_{45}) \cdot \theta_4 + (S_{45} - S_{56}) \cdot \theta_5 \quad (17)$$

where $\theta_5 = \theta_{ERd,PTF}$. S_{12}, S_{23}, S_{34}, and S_{45} are the same as in Case 1. The rotational stiffness, S_{56}, for Points 5-6, equals:

$$S_{56} = K_{fe} \cdot \left(\lambda \cdot n_{WHPu} \cdot z_u^2 + \lambda \cdot n_{WHPc} \cdot z_c^2 + \lambda \cdot n_{WHPd} \cdot z_d^2 \right) + K_{ER} \cdot n_{ERu} \cdot z_{ERu}^2 \quad (18)$$

The rotational stiffness for each of the unloading parts of the first half hysteretic loop can be derived as follows:

$$S_{67} = S_{12}; \quad S_{78} = S_{23}; \quad S_{89} = S_{34}; \quad S_{910} = S_{45}; \quad S_{1011} = S_{56} \quad (19)$$

Step 5: Column yielding avoidance

To avoid column yielding for a particular target drift (in terms of θ_t), check that the moment in the position where the column is welded on the anchor stand for θ_t is smaller than $M_{N,pl,Rd,c}$. This is ensured by the following relationship:

$$\frac{M(\theta_t)}{M_{N,pl,Rd,c}} < 1 \quad (20)$$

where $M(\theta_t)$ is the moment developed in the column base for θ_t, determined below (Eqs. (25) and (31)). If Relation (20) is not satisfied, return to Step 1 and repeat Steps 1 to 5 with a lower $M_{IGO}/M_{N,pl,Rd,c}$ ratio until the latter relationship is satisfied.

2.4 Analytical model

2.4.1 Case 1 analytical model

The values of θ at Points 2 to 4 (Fig. 5(a)) are derived from Step 3. θ_5 equals θ_t. The values of θ at Points 6 to 9 are defined as follows:

$$\theta_6 = \theta_5 - 2\cdot\theta_2;\ \ \theta_7 = \theta_5 - 2\cdot\theta_3;\ \ \theta_8 = \theta_5 - 2\cdot\theta_4 \tag{21}$$

The moment resistance of the column base at the characteristic points of Fig. 5a equals:

$$M_2 = M_{IGO} = M_D + S_{12}\cdot\theta_2 \tag{22}$$

$$M_3 = M_D + \left(S_{12} - S_{23}\right)\cdot\theta_2 + S_{23}\cdot\theta_3 \tag{23}$$

$$M_4 = M_D + \left(S_{12} - S_{23}\right)\cdot\theta_2 + \left(S_{23} - S_{34}\right)\cdot\theta_3 + S_{34}\cdot\theta_4 \tag{24}$$

$$M_5 = M_D + \left(S_{12} - S_{23}\right)\cdot\theta_2 + \left(S_{23} - S_{34}\right)\cdot\theta_3 + \left(S_{34} - S_{45}\right)\cdot\theta_4 + S_{45}\cdot\theta_5 \tag{25}$$

$$M_6 = M_D + \left(-S_{12} - S_{23}\right)\cdot\theta_2 + \left(S_{23} - S_{34}\right)\cdot\theta_3 + \left(S_{34} - S_{45}\right)\cdot\theta_4 + S_{45}\cdot\theta_5 \tag{26}$$

$$M_7 = M_D + \left(S_{23} - S_{12}\right)\cdot\theta_2 + \left(-S_{23} - S_{34}\right)\cdot\theta_3 + \left(S_{34} - S_{45}\right)\cdot\theta_4 + S_{45}\cdot\theta_5 \tag{27}$$

$$M_8 = M_D + \left(S_{23} - S_{12}\right)\cdot\theta_2 + \left(S_{34} - S_{23}\right)\cdot\theta_3 + \left(-S_{34} - S_{45}\right)\cdot\theta_4 + S_{45}\cdot\theta_5 \tag{28}$$

$$M_9 = M_D + \left(S_{23} - S_{12}\right)\cdot\theta_2 + \left(S_{34} - S_{23}\right)\cdot\theta_3 + \left(S_{45} - S_{34}\right)\cdot\theta_4 \tag{29}$$

In this case, the moment M_9 is referred to as gap-closing moment.

2.4.2 Case 2 analytical model

The values of θ at Points 2 to 4 (Fig. 6(a)) are the same with those of Case 1. θ_5 is equal to $\theta_{ERd,PTF}$ and θ_6 takes values between θ_5 and θ_t. The values of θ at the characteristic Points 7 to 11, are defined as follows:

$$\theta_7 = \theta_6 - 2\cdot\theta_2;\ \ \theta_8 = \theta_6 - 2\cdot\theta_3;\ \ \theta_9 = \theta_6 - 2\cdot\theta_4;\ \ \theta_{10} = \theta_6 - 2\cdot\theta_5 \tag{30}$$

The moment resistance of the column base at the characteristic points of Fig. 6(a), are the same with those of Case 1 up to M_5. The moment values from Point 6 onwards are defined as follows:

$$M_6 = M_D + (S_{12} - S_{23}) \cdot \theta_2 + (S_{23} - S_{34}) \cdot \theta_3 + (S_{34} - S_{45}) \cdot \theta_4 + (S_{45} - S_{56}) \cdot \theta_5 + S_{56} \cdot \theta_6 \quad (31)$$

$$M_7 = M_D - (S_{12} + S_{23}) \cdot \theta_2 + (S_{23} - S_{34}) \cdot \theta_3 + (S_{34} - S_{45}) \cdot \theta_4 + (S_{45} - S_{56}) \cdot \theta_5 + S_{56} \cdot \theta_6 \quad (32)$$

$$M_8 = M_D - (S_{12} - S_{23}) \cdot \theta_2 - (S_{23} - S_{34}) \cdot \theta_3 + (S_{34} - S_{45}) \cdot \theta_4 + (S_{45} - S_{56}) \cdot \theta_5 + S_{56} \cdot \theta_6 \quad (33)$$

$$M_9 = M_D - (S_{12} - S_{23}) \cdot \theta_2 - (S_{23} - S_{34}) \cdot \theta_3 - (S_{34} - S_{45}) \cdot \theta_4 + (S_{45} - S_{56}) \cdot \theta_5 + S_{56} \cdot \theta_6 \quad (34)$$

$$M_{10} = M_D - (S_{12} - S_{23}) \cdot \theta_2 - (S_{23} - S_{34}) \cdot \theta_3 - (S_{34} - S_{45}) \cdot \theta_4 - (S_{45} + S_{56}) \cdot \theta_5 + S_{56} \cdot \theta_6 \quad (35)$$

$$M_{11} = M_D - (S_{12} - S_{23}) \cdot \theta_2 - (S_{23} - S_{34}) \cdot \theta_3 - (S_{34} - S_{45}) \cdot \theta_4 - (S_{45} - S_{56}) \cdot \theta_5 \quad (36)$$

In Case 2, the gap-closing moment is the moment M_{11}.

3 Three-dimensional nonlinear Abaqus FEM model for the column base

A three-dimensional FEM model of the column base was developed in the software Abaqus. This model, referred to as Abaqus FEM model, realizes a specific column base design that was derived using the design procedure of Section 2.3 for M_D/M_{IGO} and $M_{IGO}/M_{N,pl,Rd,c}$ ratios equal to 0.7 and 0.6, respectively; a column axial force, N, equal to 872.24 kN; and a HEB650 steel column section. Table 1 summarises the details of the aforementioned column base design. T was calculated as 615.30 kN.

Table 1 Design details of the column base*

WHPs							
Number of elements		D_e (mm)	D_i (mm)	L_{WHP} (mm)	r (mm)	Lever arms	
Symbol	Value					Symbol	Value (mm)
n_{WHPu}	2	32	22	60	5	z_u	959.55
n_{WHPd}	2	32	22	60	5	z_d	309.55
n_{WHPc}	4	32	22	60	5	z_c	325

Tendons						
Number of elements		D_{ER}	T	L_{ER}	Lever arms	
Symbol	Value	(mm)	(kN)	(m)	Symbol	Value (mm)
n_{ERu}	2	47	615.30	7.5	z_{ERu}	796
n_{ERd}	2	47	615.30	7.5	z_{ERd}	146

Steel ducts			
Number of elements	Diameter, D_{duct} (mm)	Tube thickness, t_{duct} (mm)	Length, L_{duct} (mm)
4	114.3	6	6640

Steel plated elements							
Element	Number of elements	Length		Width		Thickness	
		Symbol	Value (mm)	Symbol	Value (mm)	Symbol	Value (mm)
Anchor stand	1	L_{as}	1348	b_{as}	1348	t_{as}	60
Anchor stand stiffeners	8	L_{sas}	307	h_{sas}	367	t_{sas}	60
Shear bumpers	4	L_{sb}	580	h_{sb}	110	t_{sb}	50
Web plates	4	L_{wp}	369.55	h_{wp}	340	t_{wp}	100
Supporting plates	8	L_{sp}	413	h_{sp}	120	t_{sp}	64
Base plate	1	h_{bp}	1607	h_{bp}	1607	t_{bp}	50
Foot end plate	1	-	650	-	650	t_{fep}	50

CFT			
Number of elements	L_{CFT} (mm)	h_{CFT} (mm)	Width (mm)
1	810	650	650

* The notation of Table 1 refers to Figs 7, 4 and 3b.

3.1 Model for the WHPs

A large number of simulations were conducted to identify the optimum mesh refinement of a single WHP. The final mesh of a single WHP, which is shown in Fig. 8, consists of three-dimensional eight-node linear hexahedral solid elements with reduced integration (C3D8R),

available in Abaqus. These C3D8R elements had a maximum side length of 8 mm at the external parts of the WHP and a minimum side length of 3 mm at its internal parts.

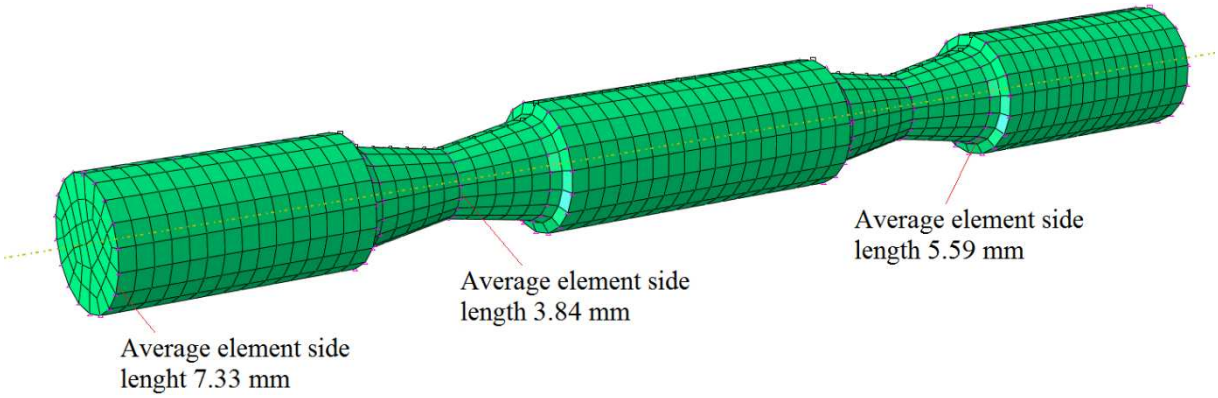

Fig. 8 Mesh of a WHP

Duplex stainless steel (SSD) material was used for the WHPs to exploit its superior seismic performance [35] and achieve the required strength, while at the same time keeping the WHP dimensions relatively small. The material model for the SSD was according to the average values of the coupon tests conducted in Vasdravellis et al. [35]; it has a yield stress equal to 543 MPa, ultimate stress equal to 778 MPa, elongation at fracture 34% and Young modulus equal to 228 MPa.

Fig. 9 shows the deformed shape of the three WHP groups and plots the equivalent plastic strain (PEEQ in Abaqus) distribution for a θ equal to 0.028 rad, under the displacement loading history described in the next section (Section 3.2); $\varphi \approx \theta$ in Fig. 9(c). From the FEM analysis, it is observed that in all three groups the stresses are more prominent in Area 2 than in Area 1. This is consistent with the experimental findings of [35] and numerical findings of [45].

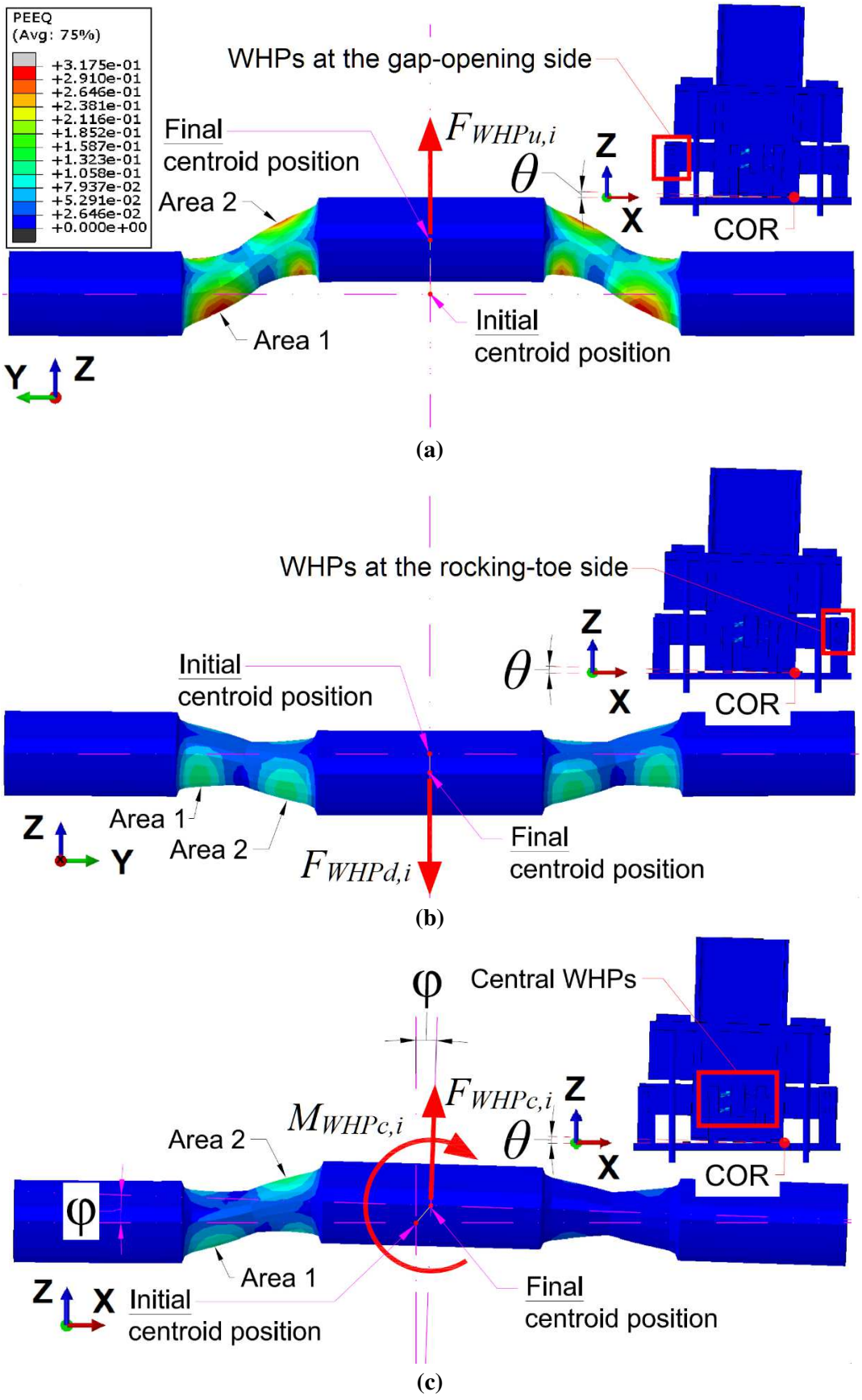

Fig. 9 PEEQ distribution in the WHPs: (a) WHP at the gap-opening side; (b) WHP at the rocking-toe side; and (c) central WHP. The index *i* in the forces and moments notation denotes one WHP

Moreover, despite that the central WHPs were farther from the COR compared to the WHPs at the rocking-toe side and, thus, were expected to develop higher stresses due to their larger lever arms, their out-of-plane loading resulted in smaller peak stresses. Lastly, it is seen that the optimized hourglass shape of the WHPs avoids stress concentrations and results in uniform distribution of plastic deformation in the internal parts, while the external parts remain elastic.

3.2 Model for the column base

Fig. 10 shows the Abaqus FEM model for the column base. A change in the length of the tendons of 14.10 mm (adjust length bolt load method of Abaqus) was applied at each tendon to model *T*; an axial pressure of a magnitude 30.39 N/mm^2 was applied at the upper cross-sectional surface of the column tip to model *N*; and a displacement-controlled boundary condition was imposed at the central node of the column tip to simulate the displacement loading history, which consisted of 45 mm amplitude half cycles.

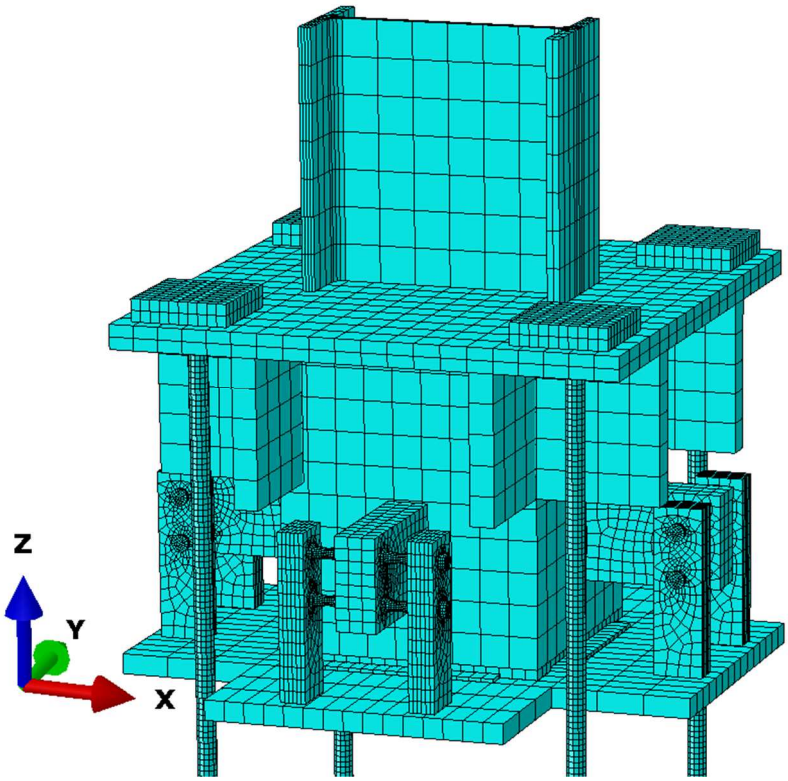

Fig. 10 Mesh of the three-dimensional Abaqus FEM model of the column base

To model the welded interfaces, kinematic tie constraints were applied to the degrees of freedom of the nodes between the supporting plates and the base plate; the anchor stand stiffeners, the anchor stand and the CFT; the web plates and the CFT; the column and the anchor stand; and the anchor stand and the CFT. Kinematic tie constraints were applied between the shear bumpers and base plate, and, the tendon washer plates (Fig. 1) and tendons. Contact interactions with normal 'hard' contact were specified between surface pairs that separate after contact. These pairs are the tendons and anchor stand holes; the tendon washer plates and anchor stand; and the shear bumpers and CFT. Between the foot end plate and base plate, and, the WHPs, web plates and supporting plates, both normal hard contact and friction were applied with a friction coefficient equal to 0.2 [7,45]. The mechanical-type full fixity boundary conditions were applied at all degrees of freedom at the underside surface of the base plate and the bottom cross-sectional surfaces of the tendons.

All the parts of the column base were modelled using C3D8R elements. In general, a finer mesh was applied to regions with the likelihood of large plastic deformations and buckling, while a coarser mesh to regions that were expected to be elastic.

The nominal stress-strain curves from coupon tests [35] were converted into true stress-plastic strain curves. For the base plate, shear bumpers, foot end plate, CFT, anchor stand, anchor stand stiffeners, tendon washer plates, web plates, supporting plates, and column, a S355 steel grade with an elasto-plastic law and isotropic hardening rule was used. The material of the tendons had nominal yield strength equal to 1050 MPa, modulus of elasticity 205 GPa, and elongation capacity 7%.

3.3 Assessment of the Abaqus FEM model for the column base

Fig. 11 shows a comparison of the M-θ behaviour of the Abaqus FEM (Section 3.2) and analytical (Section 2.4) models for the column base. In general, the results of the analyses show a good agreement between the two models. The analytical and numerical predictions of M_D and

M_{IGO} are almost the same. The elastic stiffness between the Abaqus FEM and analytical models is also identical. A slight difference is observed in the post-elastic stiffness (i.e., after Point 4 in Fig. 5(a)) of the two models because all the components of the Abaqus FEM model, except for the tendons and WHPs (which have an elastoplastic force-displacement behaviour), were modelled to have an elastic behaviour, as opposed to the analytical model where the corresponding components were considered to behave rigidly.

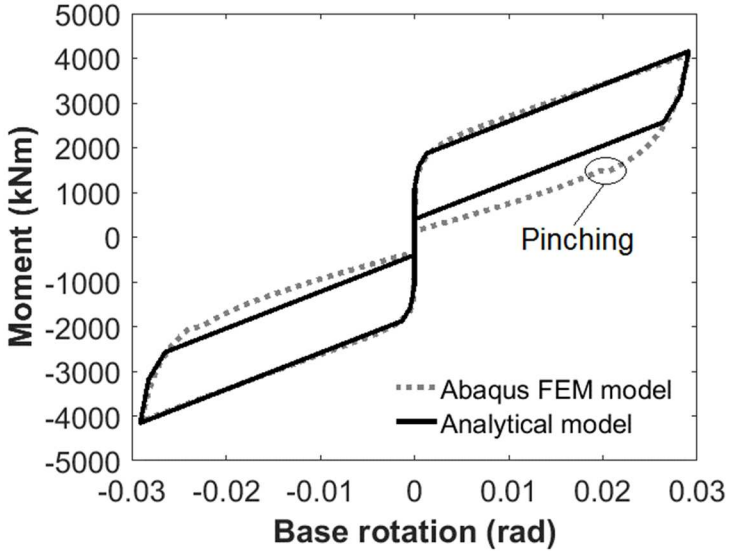

Fig. 11 Comparison of the hysteretic behaviour of the column base from the Abaqus FEM and analytical model

The analysis results show that the Abaqus FEM model predicts self-centering behaviour. Small differences are observed between the analytically and numerically predicted gap-closing moments. The differences are due to the different energy dissipation between the two models. The first reason for these differences is that the analytical model does not account for frictional energy dissipation. The second reason is because the FEM behaviour of the central WHPs in the column base differs from their analytical behaviour. This is due to the out-of-plane loading of the central WHPs in the Abaqus FEM model (Fig. 9(c)), contrary to the in-plane loading assumed for the development of the analytical model for the WHPs in [22]. The third reason is because automatic stabilization schemes were used in FEM analysis to overcome numerical convergence

issues. These schemes introduce damping forces, which slightly increase the hysteretic energy of the Abaqus FEM model.

Apart from the plastic deformations in Areas 1 and 2 of the WHPs (Fig. 9), plastic deformations are observed at the holes and bottoms of the supporting plates, as shown in Fig. 12.

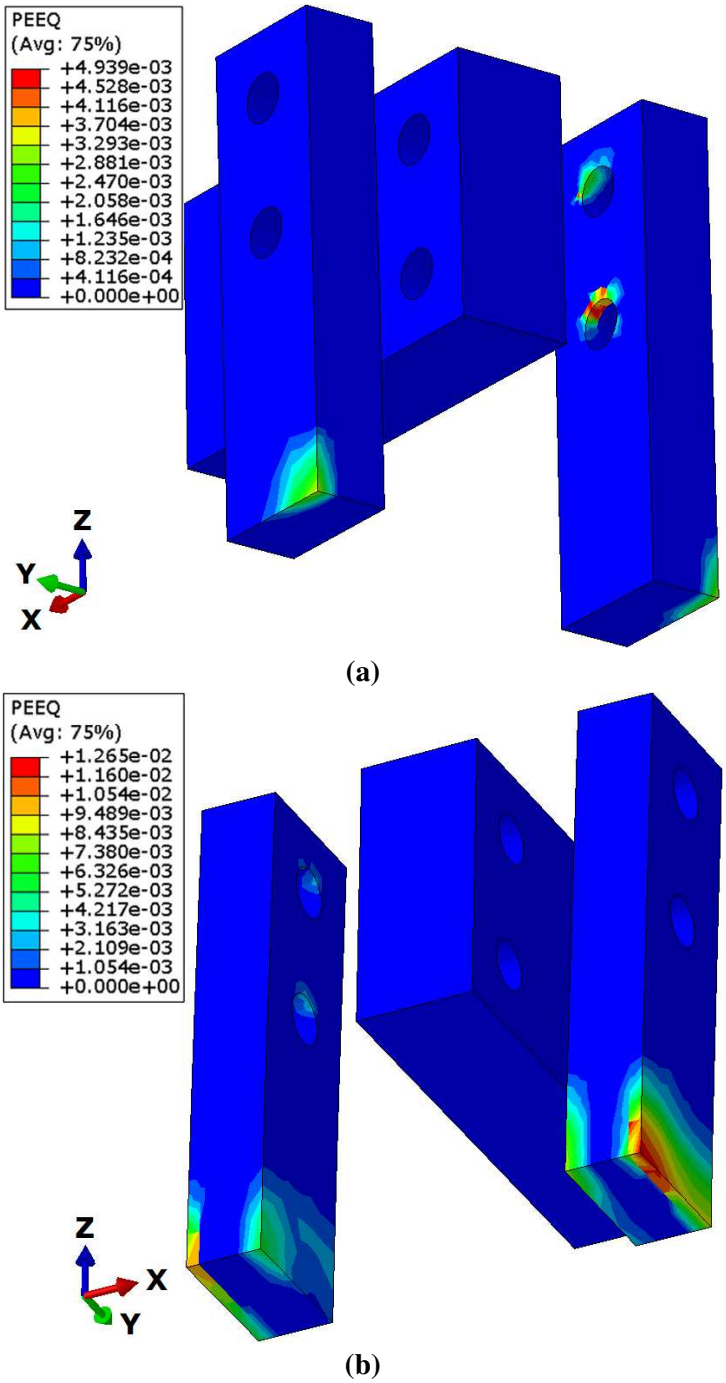

Fig. 12 PEEQ concentration areas in the web plates and supporting plates of the column base for θ=0,028 rad: (a) at the gap-opening side; and (b) at the central WHPs

However, Vasdravellis et al. [45] showed that these concentrations of plastic deformation do not affect the behaviour of the connection. Plastic deformations in the other parts of the column base and local buckling phenomena in the column are not observed. Thus, the presumption of Section 2.1, i.e., that the column base can avoid the undesirable axial shortening and concurrent loss of post-tensioning in its tendons, is confirmed. The Abaqus FEM model captures well the slight pinching effect due to the hysteretic behaviour of the WHPs. Pinching is seen as a small flat region in the unloading parts of the curves in Fig. 11 and is caused by the slight ovalization of the supporting plate holes under the bearing forces of the external parts of the WHPs.

4 OpenSees FEM model for the column base

4.1 Model for the column base

A two-dimensional FEM model for the column base was developed in OpenSees [26] and used for the seismic performance evaluation of buildings using the column base (Section 5). This model is referred to as OpenSees FEM model and is shown in Fig. 13.

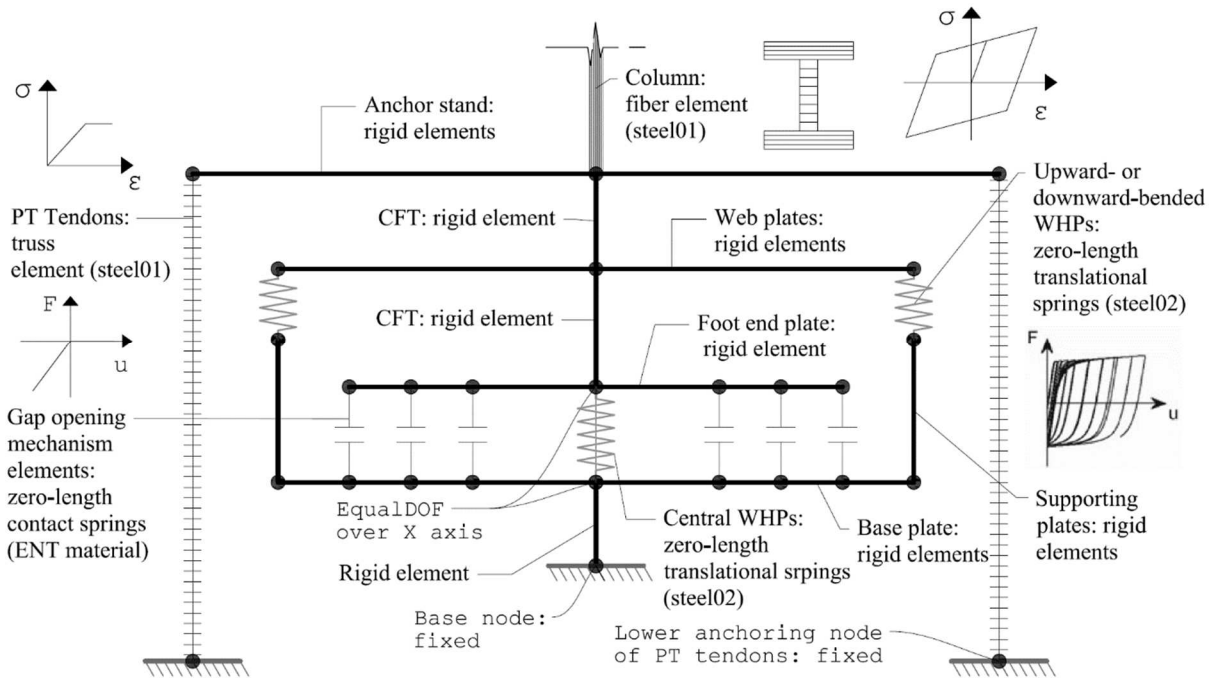

Fig. 13 Two-dimensional OpenSees FEM model for the column base

The column was modelled with nonlinear force-based fiber elements. The fibers are associated with the Steel01 material of OpenSees for 355 MPa yield strength and 0.002 post-yield stiffness ratio. Rigid elastic beam-column elements were used to model the rocking interface, CFT and anchor stand. Rocking was simulated by using three zero-length translational contact springs placed at equal distances along the left and right half-depth-part of the CFT cross-section. These springs were associated with the ENT material in OpenSees, which exhibits an elastic compression-no tension force-displacement behaviour. The compression stiffness of these springs was set equal to twenty times the axial stiffness of the column, based on the approach of [46]. Each WHP group was modelled with one zero-length hysteretic spring placed at the geometric centre of the group. This spring follows a smooth Giuffre-Menegotto-Pinto hysteretic rule with isotropic hardening. The tendons were modelled as truss elements. These elements had a cross-sectional area equal to A_{ER} and material with bilinear elastoplastic hysteresis (Steel01). To account for the initial post-tensioning, an initial strain equal to $T/(A_{ER} \cdot E_{ER})$ was imposed on each truss element.

4.2 Assessment of the OpenSees FEM model for the column base

Fig. 14 compares the hysteretic behaviour of the OpenSees FEM and analytical model.

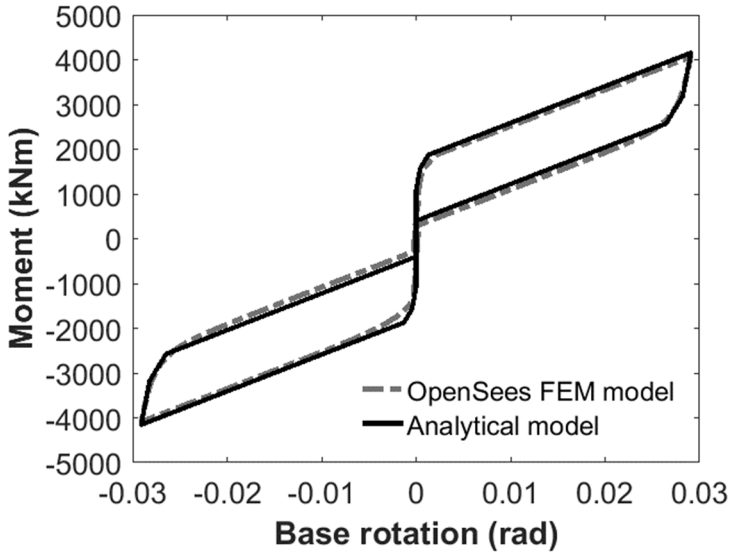

Fig. 14 Comparison of the hysteretic behaviour of the column base from the OpenSees FEM and analytical model

It is seen that the hysteretic responses of the two models are almost identical. The small differences that are observed in two hysteretic responses are because the analytical model considers as WHP lever arms the horizontal distances between the COR and the geometric centre of each WHP group (Section 2.2).

5 Prototype building and design cases

The prototype building in [44] was considered in this study. Fig. 15(a) shows the plan view of the building, which has two identical perimeter seismic-resistant frames in the X direction. The building has ductile non-structural elements, and therefore, the peak interstorey drift ratio ($\theta_{s,max}$) should be lower than 0.75% under the frequently occurred earthquake (FOE; 10% probability of exceedance in 10 years). The design basis earthquake (DBE; 10% probability of exceedance in 50 years) is expressed by the Type 1 elastic response spectrum of EC8 with peak ground acceleration equal to 0.35g and ground type B. The maximum considered earthquake (MCE) is assumed to have intensity 150% the intensity of the DBE. The study focuses on the X-axis perimeter seismic-resistant frame that is placed on the bottom of the plan view of Fig. 15(a) (Elevation A of the prototype building).

The frame of interest, the elevation of which is shown in Fig. 15(b), is designed as two different seismic-resistant systems: first, as an SC-MRF with conventional full-strength column bases, referred to as SC-MRF; and second, as an SC-MRF with the proposed column base, referred to as SC-MRF-CB.

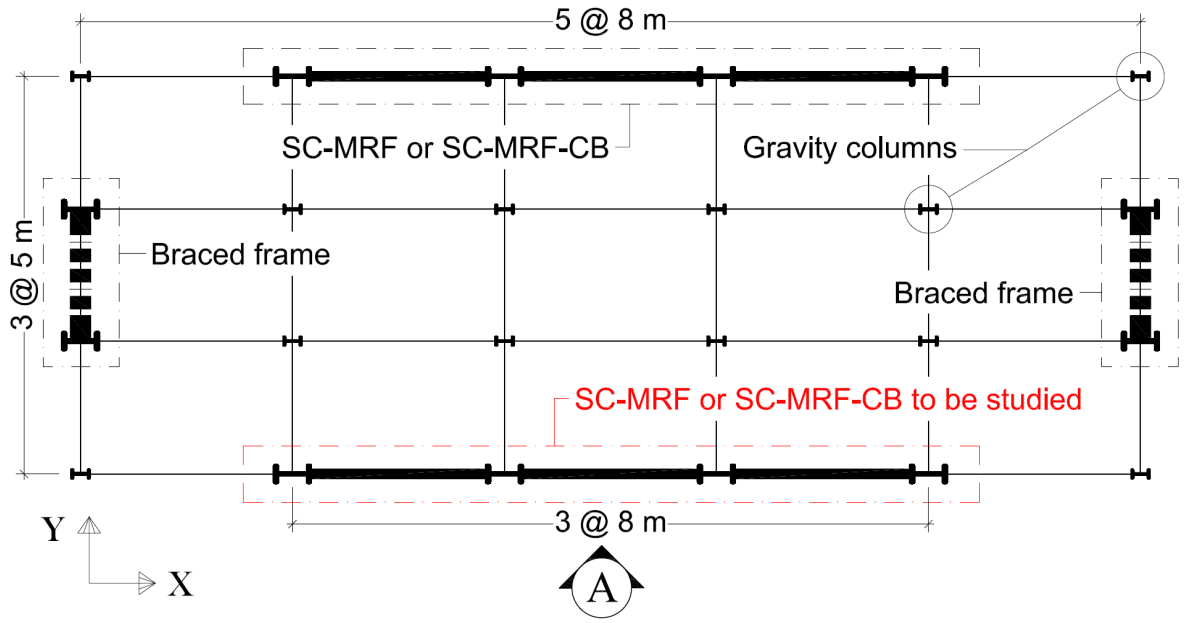

(a)

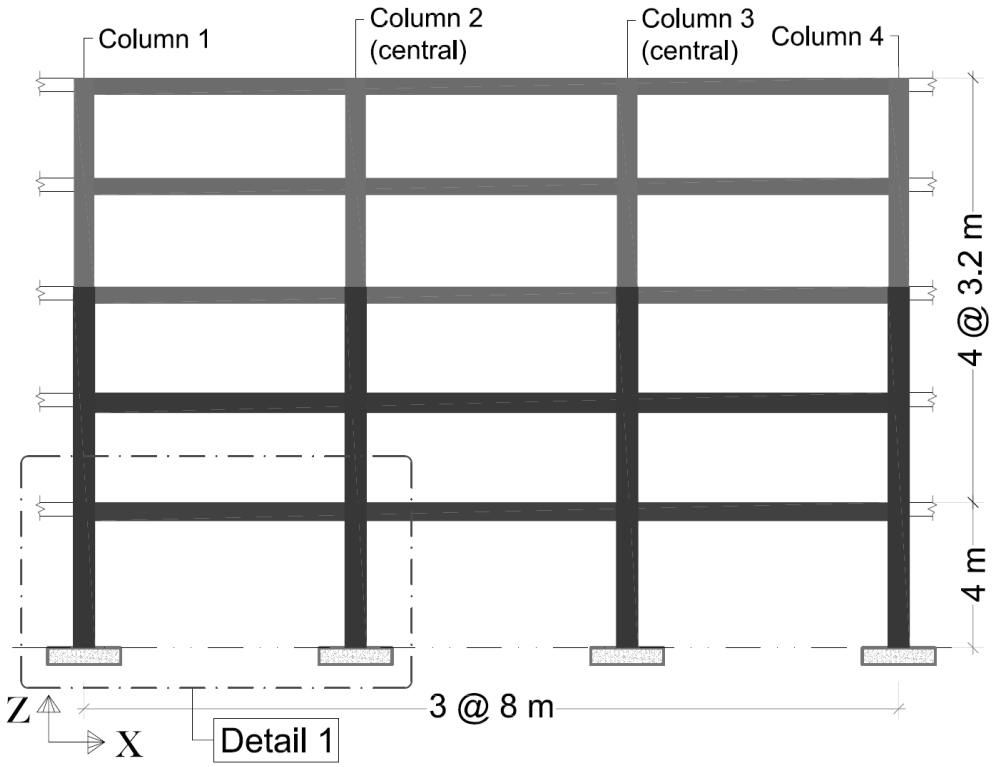

(b)

Fig. 15 (a) Plan view of the prototype building; (b) perimeter seismic-resistant frame in Elevation A of the prototype building

Fig. 16 shows the bottom-left part of the SC-MRF-CB in Elevation A of the prototype building (Detail 1 in Fig. 15(b)). The SC-MRF and SC-MRF-CB have the same cross sections,

use PT beam-column connections with WHPs (Fig. 16) [46], and were designed according to the procedure of [44]. Table 2 lists the column and beam sections of the two systems. The WHP characteristics for the PT beam-column connections of each floor in the two systems are given in Table 3, while Table 4 provides the characteristics of the beam flange reinforcing plates. Table 5 gives the size and initial PT force of the PT bars for each floor beams in the SC-MRF and SC-MRF-CB.

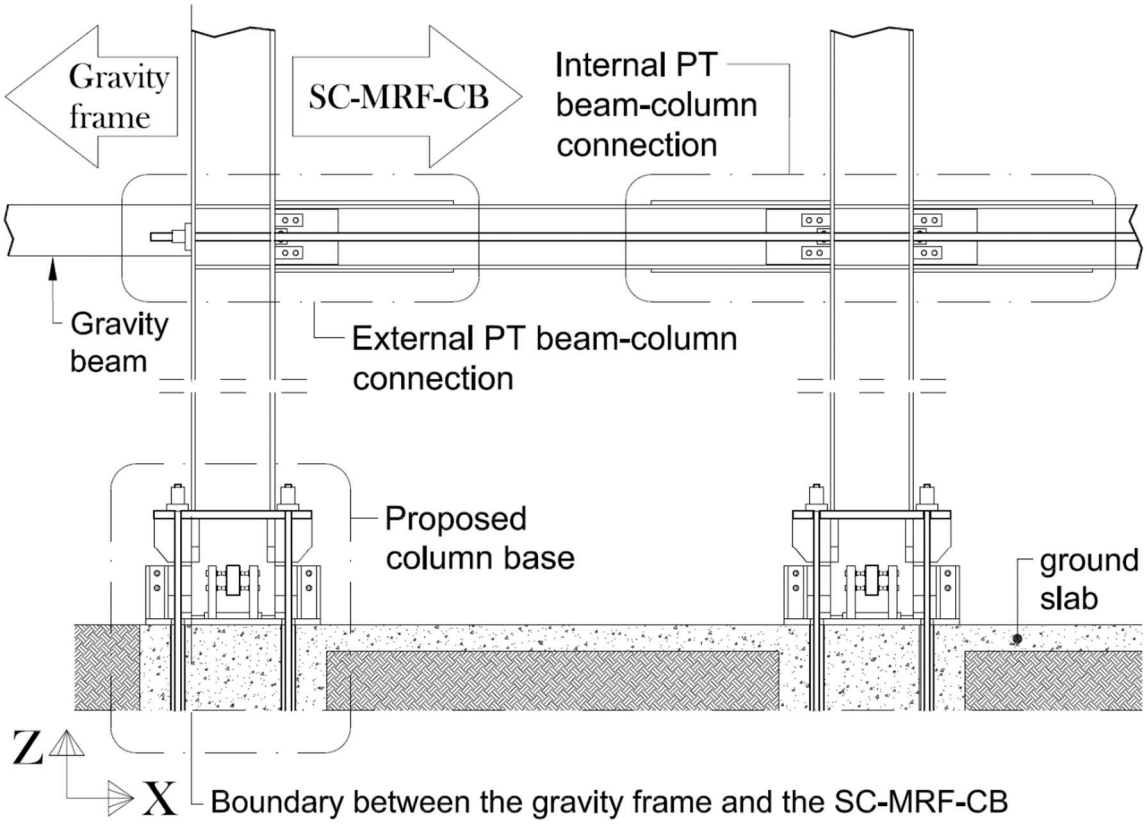

Fig. 16 Close-up view of the bottom-left part of the SC-MRF-CB in Elevation A of the prototype building (Detail 1 in Fig. 15(b))

Table 2 Beams and columns of the SC-MRF and SC-MRF-CB

Storey	**Cross sections**	
	Beams	Columns
1	IPE 550	HE 650 B
2	IPE 600	HE 650 B
3	IPE 550	HE 650 B
4	IPE 500	HE 600 B
5	IPE 500	HE 600 B

Table 3 Dimensions and yield stress ($f_{y,WHP}$) of the WHPs in the PT beam-column connections of the SC-MRF and SC-MRF-CB

Storey	$fy_{,WHP}$ (MPa)	L_{WHP} (mm)	D_i (mm)	D_e (mm)
1	235	70	33	43
2	235	70	36	46
3	235	70	33	44
4	235	70	30	41
5	235	70	28	39

Table 4 Reinforcing plates of the beams of the SC-MRF and SC-MRF-CB

Storey	$f_{y,rp}$ (MPa)	L_{rp} (mm)	b_{rp} (mm)	t_{rp} (mm)
1	275	1392	210	35
2	275	1660	220	46
3	275	1416	210	35
4	275	1092	200	26
5	275	743	200	22

Note: L_{rp} is the length of the reinforcing plates, b_{rp} their width, t_{rp} their thickness, and $f_{y,rp}$ their yield stress

Table 5 PT bars of the beam-column connections in the SC-MRF and SC-MRF-CB

Storey	$f_{y,PT}$ (MPa)	d_{PT} (mm)	T_0 (kN)
1	930	50	1086.93
2	930	60	1255.54
3	930	48	1086.93
4	930	38	941.226
5	930	36	941.226

Note: $f_{y,PT}$ is the yield stress of the PT bars, d_{PT} their diameter, and T_0 the initial PT force in both PT bars

The procedure described in Section 2.3 is used to design the column bases of the SC-MRF-CB. The ratios M_D/M_{IGO} and $M_{IGO}/M_{N,pl,Rd,c}$ are taken equal to 0.65 and 0.35, respectively. N is equal to 872.24 kN. The materials for the components of the column base are as follows: Duplex SS2205 stainless steel grade with 400 MPa yield stress for the WHPs; S355 steel grade for the web plates, supporting plates, anchor stand, anchor stand stiffeners, CFT, shear bumpers and base plate; and Y1050 steel grade of VSL [47] with yield stress 1634 MPa for the tendons. The design procedure of Section 2.3 resulted in: T=233.35 kN; D_e=28 mm; D_i=18 mm; L_{ER}=4.8 m; L_{duct}=3.99 m; and D_{ER}=34 mm. The rest of the design details of the rocking column bases are given in Table 1.

6 Nonlinear models of the frames

To investigate the seismic performance of the SC-MRF and SC-MRF-CB, two-dimensional frame models were developed in OpenSees. The models utilise the OpenSees model in [44] to model the PT beam-column connections in both systems. This model was validated against experimental results by Vasdravellis et al. [22] and found to accurately simulate the behaviour of the specific PT connection typology. To reliably capture the beam local buckling, irrespective of where the buckling occurs, this model uses the bilin material of OpenSees, which simulates the modified Ibarra-Krawinkler deterioration model with bilinear hysteretic response, presented in [48]. It is noted that determining whether the buckling occurs in the web or flanges of the beams is out of the scope of this research. The OpenSees FEM model of Section 4.1 is used to model the column bases of the SC-MRF-CB. To account for P-Δ effects, the gravity columns of the tributary area of the SC-MRF and SC-MRF-CB were modelled as three lean-on columns, i.e., one for each of the three bays of the two systems (Fig. 15(b)). These columns are pinned at their base and continuous along their height. The flexural and axial stiffness of each lean-on column are equal to the sum of the flexural and axial stiffness of the gravity columns that it represents.

7 Monotonic and cyclic base shear vs roof drift behaviour

Fig. 17 shows the base shear coefficient (V/W; V: base shear; W seismic weight of the frame)-roof drift (θ_r) behaviour of the SC-MRF-CB and SC-MRF from nonlinear monotonic static (pushover) analysis under an inverted triangular force distribution. The graphs also indicate the structural limit states and θ_r estimations under the FOE, DBE and MCE.

Fig. 17(a) shows the pushover curve of the SC-MRF. A column plastic hinge occurs at θ_r=1.84%, i.e., above the DBE roof drift limit (1.61%). The first beam plastic hinge occurs at θ_r=2.00%. The first beam local buckling occurs at θ_r=3.51%. After this point, the strength of the

SC-MRF increases up to a *V/W* equal to 0.32 at θ_r=3.98%. The last structural limit state is the PT-bar yielding at θ_r=5.02%.

Fig. 17(b) shows the pushover curve of the SC-MRF-CB. Rocking in the column bases initiates at θ_r=0.12%. The first beam plastic hinge occurs at θ_r=1.73% and the first beam local buckling at θ_r=3.35%. The strength of the system increases up to θ_r=4.22%, reaching a value of *V/W* equal to 0.33. The first PT-bar yielding in the beam-column connections occurs at θ_r=4.76%, followed by the first column plastic hinge at θ_r=4.83%, i.e., almost two times the MCE θ_r. Finally, yielding at the tendons of the column bases occurs at θ_r=5.23%.

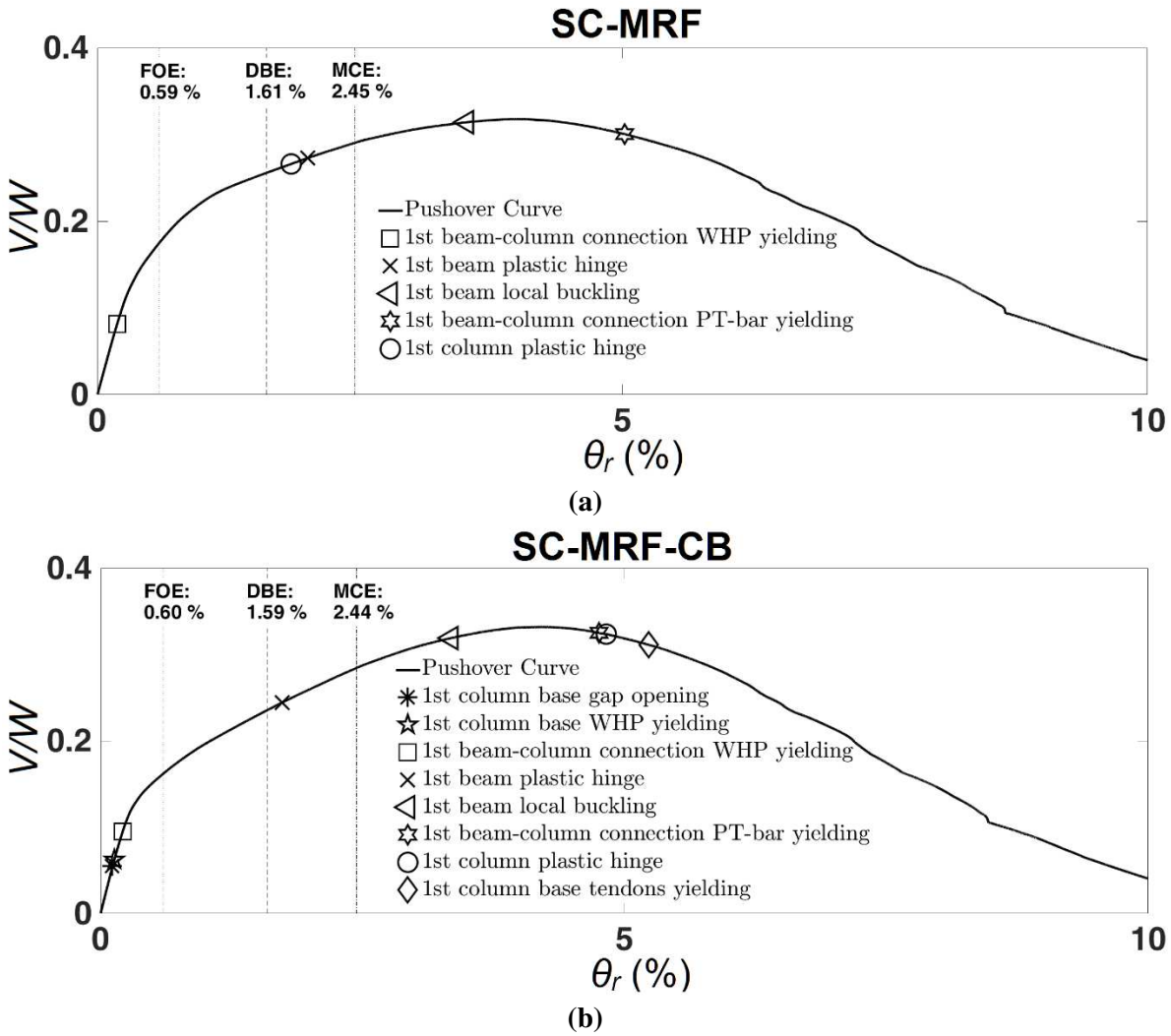

Fig. 17 Base shear coefficient-roof drift behaviours of the two design cases from nonlinear monotonic static analysis: (a) SC-MRF; and (b) SC-MRF-CB

The previous discussion shows that the SC-MRF-CB reaches the critical column plastic hinge limit state at a significantly higher (approximately 2.5 times larger) θ_r compared to that of the SC-MRF. Regarding the beam plastic hinge and beam local buckling limit states, the SC-MRF-CB exhibits a comparable performance with the SC-MRF. Moreover, the SC-MRF-CB and SC-MRF have comparable strengths.

Fig. 18 shows the V/W-θ_r behaviours of the SC-MRF and SC-MRF-CB from nonlinear cyclic (push-pull) static analysis up to the DBE θ_r. Fig. 18(a) shows that the SC-MRF has a residual θ_r of 0.18% due to column plastic hinging, while the SC-MRF-CB eliminates residual drifts and achieves a full self-centering behaviour (Fig. 18(b)).

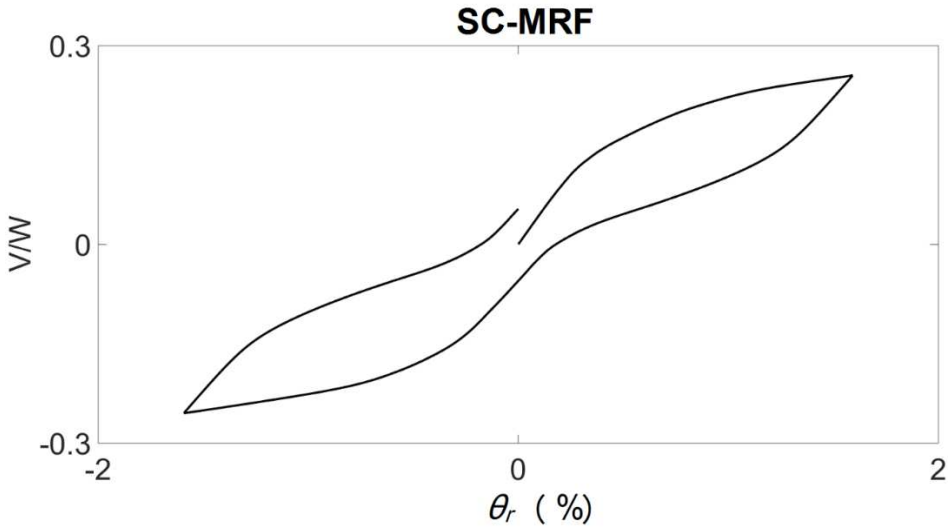

(a)

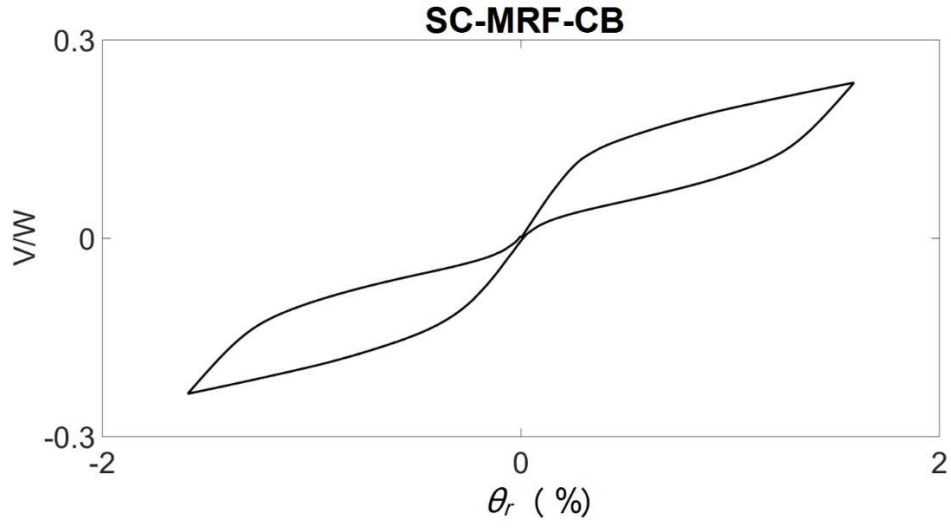

(b)

Fig. 18 Base shear coefficient-roof drift behaviours of the two design cases from nonlinear cyclic static analysis: (a) SC-MRF; and (b) SC-MRF-CB

8 Nonlinear dynamic analyses

8.1 Ground motions and procedure for dynamic analyses

A suite of 22 recorded ground motions, developed by the ATC-63 project [49], was utilized for nonlinear dynamic time-history analyses. The ground motions were recorded on stiff soil, did not exhibit pulse-type near fault characteristics and were scaled to DBE (Fig. 19) and MCE, where the seismic intensity was represented by the 5% spectral acceleration, S_a, at T of the frame models described in Section 6.

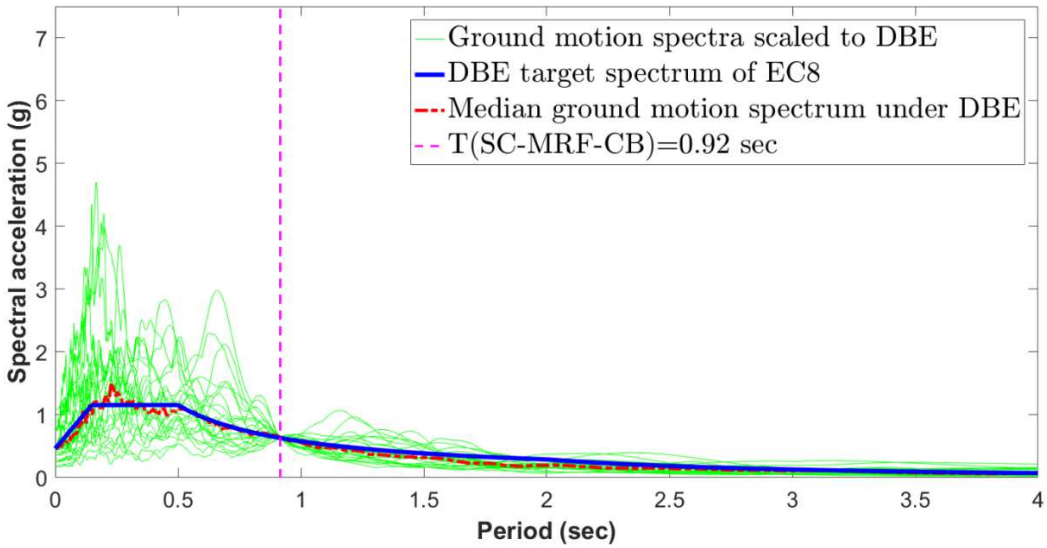

Fig. 19 Comparison of the DBE spectrum of EC8 with the scaled spectra of the ground motions used in the nonlinear dynamic analyses

The Newmark's constant average acceleration method was utilized for the integration of the equations of motion. The Newton-Raphson method with initial tangent stiffness iterations was employed to solve the nonlinear residual equations at each integration step. The time step was selected equal to 0.001 sec to enhance the convergence of the method. A Rayleigh damping matrix was used to model the inherent 3% critical damping.

8.2 Seismic assessment

The results of the 22 nonlinear response-history analyses for the two design cases were post-processed and the median $\theta_{s,max}$ and residual interstorey drift ratios ($\theta_{s,res}$) are shown in Table 6.

Table 6 Median $\theta_{s,max}$ and $\theta_{s,res}$ for the SC-MRF and SC-MRF-CB from nonlinear dynamic analyses

Seismic-resistant system	**System weight**	**Fundamental period**	**Damping ratio**	$\theta_{s,max}$* (%)		$\theta_{s,res}$* (%)	
	W (kN)	T_1 (sec)	ξ (%)	DBE	MCE	DBE	MCE
SC-MRF	10790,71	0.97	3	1.5816	2.2855	0.0405	0.1141
SC-MRF-CB	10790,71	0.92	3	1.1659	1.9035	0.0003	0.0011

* All the values are rounded off to four decimal digits

Fig. 20 shows the comparison of the height-wise distribution of $\theta_{s,max}$ for the SC-MRF and SC-MRF-CB under the DBE and MCE.

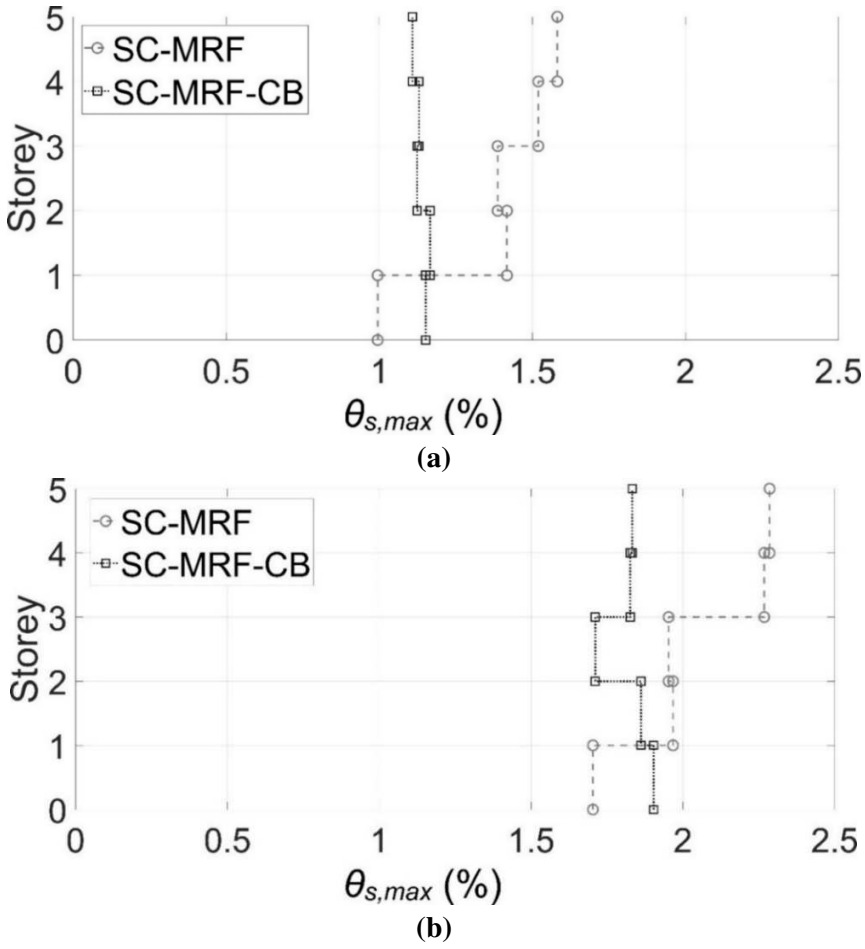

Fig. 20 Comparison of the median height-wise distribution of the peak interstorey drift ratios of the SC-MRF and SC-MRF-CB under the: (a) DBE; and (b) MCE

The SC-MRF-CB has $\theta_{s,max}$ 26% and 17% lower than that of the SC-MRF under the DBE and MCE, respectively. This is due to the CFT of the proposed column base, which decreases the flexible length of the first-storey columns, and thus, reduces the period of the SC-MRF-CB (Table 6).

Fig. 21 shows the height-wise distribution of $\theta_{s,res}$ for the SC-MRF and SC-MRF-CB under the DBE and MCE.

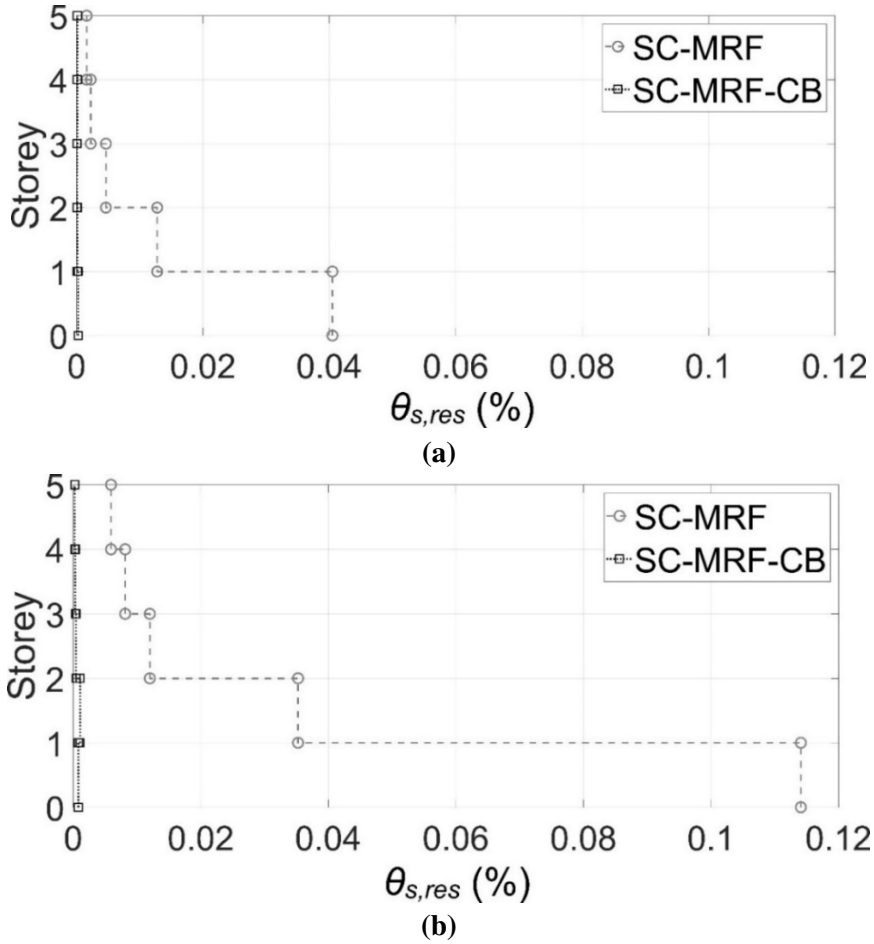

Fig. 21 Comparison of the median height-wise distribution of the residual interstorey drift ratios of the SC-MRF and SC-MRF-CB under the: (a) DBE; and (b) MCE

It can be seen that the SC-MRF-CB has $\theta_{s,res}$ 99% lower than those of the SC-MRF under both the DBE and MCE.

Fig. 22 and Fig. 23 show the stress-strain response-history in the flange of a first-storey column in the SC-MRF and SC-MRF-CB, respectively, under a specific earthquake ground motion scaled to DBE and MCE. The results shown in the aforementioned figures are representative of all the ground motions used in the analyses.

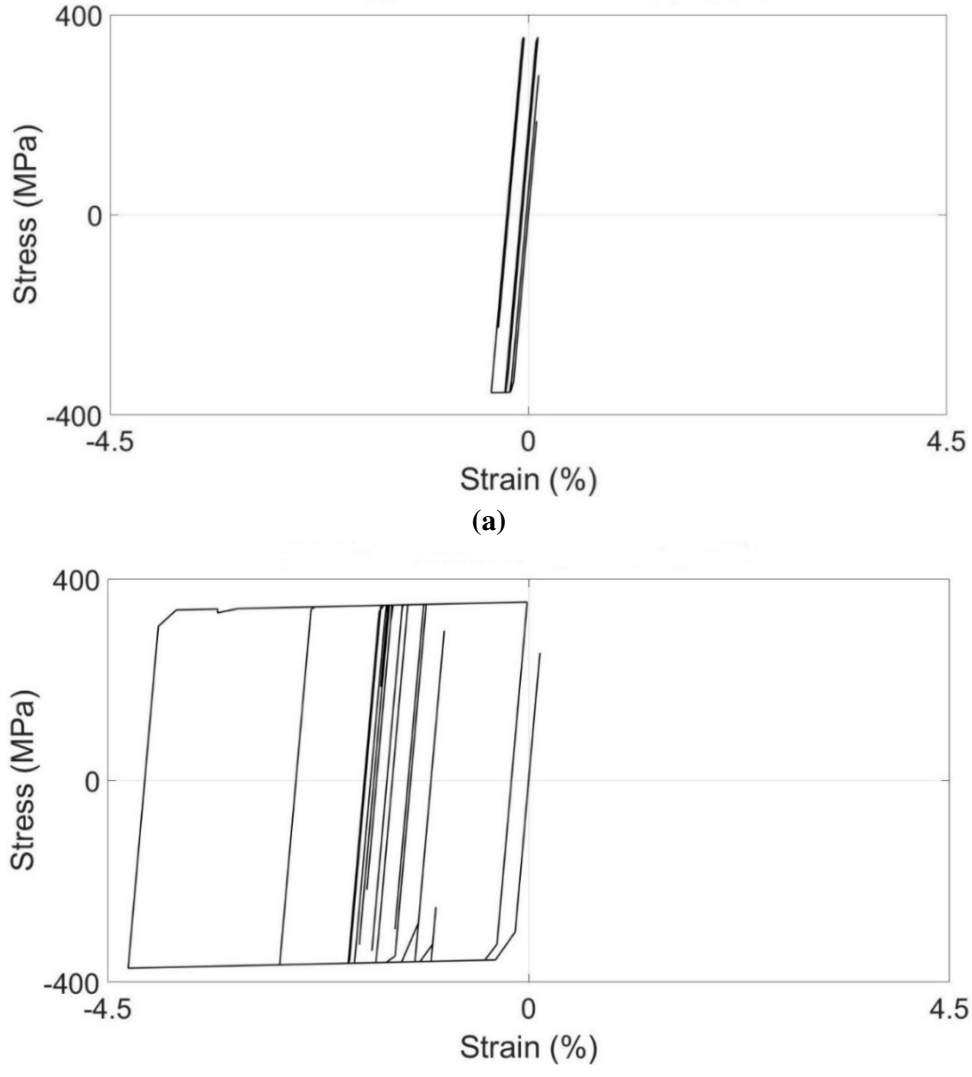

Fig. 22 Stress-strain response-history plots of a flange of a first-storey column in the SC-MRF, under the 1990 Manjil, Iran earthquake, scaled to: (a) DBE; and (b) MCE

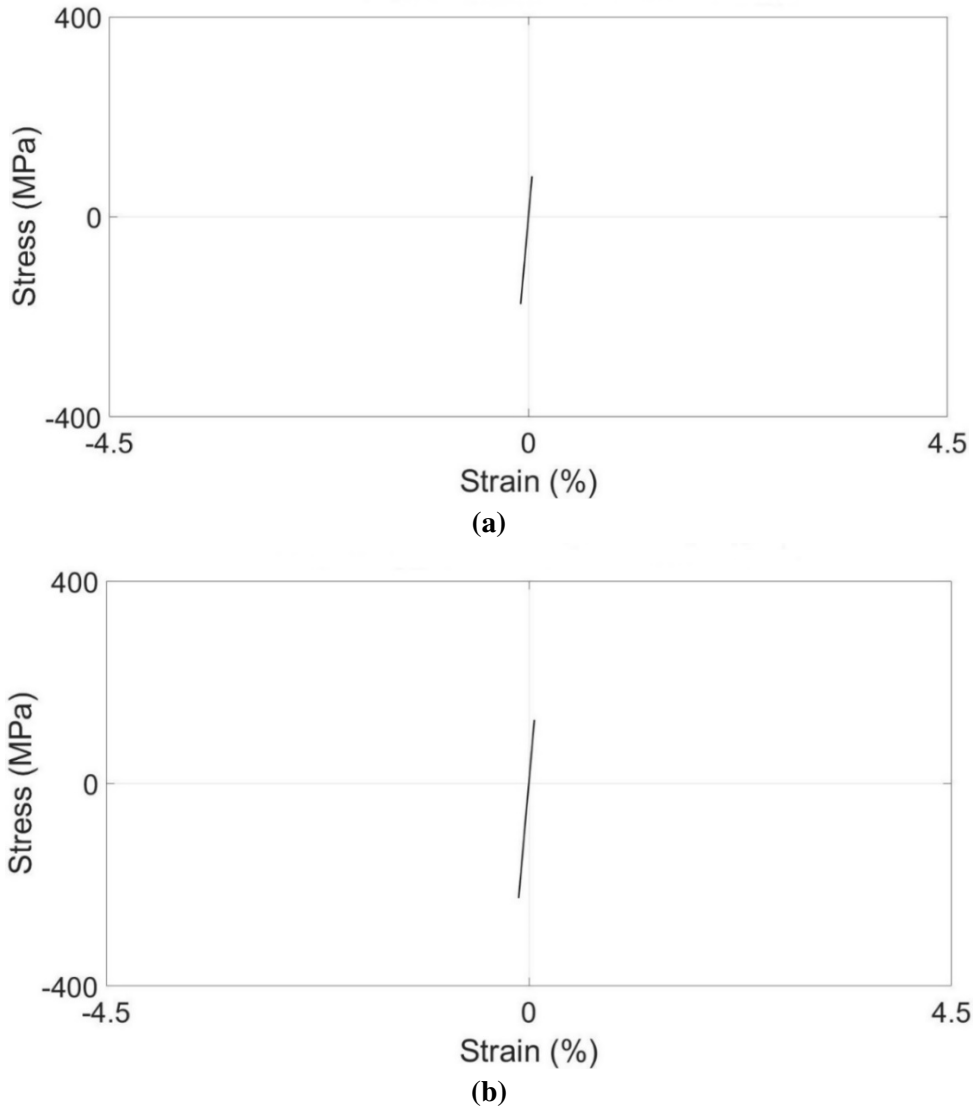

Fig. 23 Stress-strain response-history plots of a flange of a first-storey column in the SC-MRF-CB, under the 1990 Manjil, Iran earthquake, scaled to: (a) DBE; and (b) MCE

As it can be seen from the above figures, the column in the SC-MRF experiences plastic deformations both under the DBE and MCE, while in the SC-MRF-CB these plastic deformations are avoided. Thus, the proposed column base protects the first-storey columns from yielding and drastically reduces the $\theta_{s,res}$ of the first storey.

9 Summary and conclusions

This paper proposes a self-centering steel column base with high-strength steel post-tensioned (PT) tendons and hourglass shape steel yielding devices (WHPs). The following conclusions are drawn:

- Damage is concentrated within the replaceable WHPs, while the rest of the column base is expected to remain damage-free. The column base allows for multiple arrangements of the PT tendons outside the perimeter of the column section. This feature, coupled with selecting appropriate characteristics for the tendons and WHPs allows for the independent tuning of the moment resistance, rotational stiffness, and self-centering capability of the column base. Furthermore, the proposed column base exhibits increased rotation capacity compared to its conventional counterpart, and avoids column axial shortening and loss of post-tensioning.
- An analytical model and an associated design procedure are presented to predict the hysteretic behaviour and all structural limit states of the proposed column base.
- The behaviour of the column base has been assessed with detailed three-dimensional nonlinear finite element method (FEM) models in the software Abaqus, while its effect on the seismic response of a steel building has been quantified by nonlinear dynamic analysis in the software OpenSees. The FEM models predict and simulate well the hysteretic behaviour of the column base. The results of the FEM models are in good agreement with the analytical model and show that the column base can avoid non-repairable damage even under very large rotations. Under such rotations, small inelastic deformations may be developed at the holes and bottoms of the supporting plates without affecting the behaviour of the column base.

- The results of nonlinear dynamic analyses show that the column base protects the first-storey columns from yielding and drastically reduces the first-storey residual drifts under the design and maximum considered earthquake intensities.

Acknowledgments

Financial support for this work was provided by the Engineering and Physical Science Research Council of the United Kingdom (EPSRC); Award Ref.: 1500450.

References

[1] A. Aviram, B. Stojadinovic, A. Der Kiureghian, Performance and reliability of exposed column base plate connections for steel moment-resisting frames, Berkeley, CA, USA, 2010.

[2] J. Ruiz-García, A. Kanvinde, Effect of column base flexibility on residual drift demands of low-rise steel moment-resisting frames, in: 2013 World Congr. Adv. Struct. Eng. Eng. Mech. (ASEM13), Sept. 8-12, Jeju, Korea, 2013: pp. 627–639.

[3] F. Zareian, A. Kanvinde, Effect of column-base flexibility on the seismic response and safety of steel moment-resisting frames, Earthq. Spectra. 29 (2013) 1537–1559. doi:10.1193/030512EQS062M.

[4] C.-C. Chou, J.-H. Chen, Analytical model validation and influence of column bases for seismic responses of steel post-tensioned self-centering MRF systems, Eng. Struct. 33 (2011) 2628–2643. doi:10.1016/j.engstruct.2011.05.011.

[5] M. Eröz, D.W. White, R. DesRoches, Direct analysis and design of steel frames accounting for partially restrained column base conditions, J. Struct. Eng. 134 (2010) 1508–1517. doi:10.1061/(ASCE)0733-9445(2008)134:9(1508).

[6] BS EN 1998-1, Eurocode 8: Design of structures for earthquake resistance - Part 1:

General rules, seismic actions and rules for buildings., 2013.

[7] BS EN 1993-1-8, Eurocode 3 : Design of steel structures — Part 1-8 : Design of joints, United Kingdom, 2010.

[8] R.W. Clough, A.A. Huckelbridge, Preliminary Experimental Study of Seismic Uplift of a Steel Frame, 1977.

[9] M. Long, C. Bergad, Analysis of Rotational Column with Plastic Hinge, in: 2004 Annu. Tri-Center Earthq. Eng. Symp. Young Res., MCEER, Kiawah Island Golf Resort, Charleston, South Carolina, 2004: pp. 183–195. https://mceer.buffalo.edu/education/reu/04Proceedings/12Long_Bergad.pdf.

[10] T. Takamatsu, H. Tamai, Non-slip-type restoring force characteristics of an exposed-type column base, J. Constr. Steel Res. 61 (2005) 942–961. doi:10.1016/j.jcsr.2005.01.003.

[11] T. Takamatsu, H. Tamai, T. Yamanishi, Self-centering performance of non-slip-type exposed column base, in: A.W. Federico Mazzolani (Ed.), 5th Int. Conf. Behav. Struct. Seism. Areas, STESSA 2006, August 14-17, CRC Press, Taylor & Francis Group, Yokohama, Japan, 2006: pp. 357–362.

[12] M. Midorikawa, T. Azuhata, T. Ishihara, A. Wada, Shaking table tests on seismic response of steel braced frames with column uplift, Earthq. Eng. Struct. Dyn. 35 (2006) 1767–1785. doi:10.1002/eqe.603.

[13] T. Yamanishi, K. Kasai, T. Takamatsu, H. Tamai, Innovative Column-Base Details Capable of Tuning Rigidity and Strength for Low to Medium-Rise Steel Structures, in: 15th World Conf. Earthq. Eng., Lisbon, Portugal, 2012.

[14] H. Chi, J. Liu, Seismic behavior of post-tensioned column base for steel self-centering moment resisting frame, J. Constr. Steel Res. 78 (2012) 117–130. doi:10.1016/j.jcsr.2012.07.005.

[15] J.D. Tait, G.K. Sidwell, J.F. Finnegan, Case study - Elevated apartments - A rocking 15 storey apartment building, in: Steel Innov. Conf. 2013 Christchurch, New Zeal. 21-22 Febr., 2013.

[16] J. Borzouie, G.A. Macrae, J.G. Chase, G.W. Rodgers, G.C. Clifton, Experimental studies on cyclic performance of column base weak axis aligned asymmetric friction connection, J. Constr. Steel Res. 112 (2015) 252–262. doi:10.1016/j.jcsr.2015.05.007.

[17] M. Ikenaga, M. Nakashima, T. Nagae, Reduction of residual story drift of moment resisting frame using self-centering column bases, in: Federico M. Mazzolani;James M. Ricles;Richard Sause (Ed.), Stessa 2009 - Behav. Steel Struct. Seism. Areas, Taylor & Francis Group, London, UK, Philadelphia, Pennsylvania, USA, 2009: pp. 465–471.

[18] C.-C. Chen, H.-W. Lin, R.-S. Tsai, Self-centering and energy dissipation of a post-tensioned steel column base, in: Second Eur. Conf. Earthq. Eng. Seismol. (2ECCES), 25-29 August, Istanbul, Turkey, 2014.

[19] H. Chi, J. Liu, Response of self-centering steel moment resisting frames with post-tensioned column bases under seismic loading, in: 4th Int. Conf. Earthq. Eng. Oct. 12-13, Taipei, Taiwan, 2006.

[20] M. Ikenaga, T. Nagae, M. Nakashima, K. Suita, Development of column bases having self-centering and damping capability, STESSA 2006. (2006) 703–708.

[21] G.A. MacRae, C.R. Urmson, W.R. Walpole, P. Moss, K. Hyde, C. Clifton, Axial shortening of steel columns in buildings subjected to earthquakes, Bull. New Zeal. Soc. Earthq. Eng. 42 (2009) 275–287.

[22] G. Vasdravellis, T.L. Karavasilis, B. Uy, Large-Scale Experimental Validation of Steel Post-Tensioned Connections with Web Hourglass Pins, J. Struct. Eng. 139 (2013) 1033–42. doi:10.1061/(ASCE)ST.1943-541X.0000696.

[23] V.C. Kamperidis, T.L. Karavasilis, G. Vasdravellis, Design and modeling of a novel damage-free steel column base, in: Eighth Int. Conf. Adv. Steel Struct. (ICASS 2015), Lisbon, Portugal, July 22-24, 2015: p. Paper No. 118. http://wrap.warwick.ac.uk/78241/.

[24] F. Freddi, C.A. Dimopoulos, T.L. Karavasilis, Rocking damage-free steel column base with friction devices: design procedure and numerical evaluation, Earhtquake Eng. Struct. Dyn. (2017). doi:10.1002/eqe.2904.

[25] Dassault Systèmes Simulia Corporation, Abaqus, (2013). http://www.3ds.com/products-services/simulia/products/abaqus/.

[26] U. of C. Pacific Earthquake Engineering Research Center (PEER), OpenSees, (2015). http://opensees.berkeley.edu.

[27] J.T. Hewes, M.J.N. Priestley, Seismic design and performance of precast concrete segmental bridge columns. Report No. SSRP-2001/25, La Jolla, California 92093-0085, USA, 2002.

[28] T. Guo, Z. Cao, Z. Xu, S. Lu, Cyclic load tests on self-centering concrete pier with external dissipators and enhanced durability, J. Struct. Eng. 142 (2016) 4015088. doi:10.1061/(ASCE)ST.1943-541X.0001357.

[29] C.-C. Chou, J.-H. Chen, Column restraint in post-tensioned self-centering moment frames, Earthq. Eng. Struct. Dyn. 39 (2010) 751–774. doi:10.1002/eqe.972.

[30] C.-C. Chou, Y.-C. Chen, Cyclic tests of post-tensioned precast CFT segmental bridgecolumns with unbonded strands, Earthq. Eng. Struct. Dyn. 35 (2006) 159–175. doi:10.1002/eqe.512.

[31] G. Guerrini, J.I. Restrepo, M. Massari, A. Vervelidis, Seismic Behavior of Posttensioned Self-Centering Precast Concrete Dual-Shell Steel Columns, J. Struct. Eng. 141 (2015) 4014115. doi:10.1061/(ASCE)ST.1943-541X.0001054.

[32] M.M. Garlock, J.M. Ricles, R. Sause, Experimental Studies of Full-Scale Posttensioned Steel Connections, J. Struct. Eng. 131 (2005) 438–448. doi:10.1061/(ASCE)0733-9445(2005)131:3(438).

[33] J.D. Newell, C.-M. Uang, Cyclic Behavior of Steel Wide-Flange Columns Subjected to Large Drift, J. Struct. Eng. 134 (2008) 1334–1342. doi:10.1061/(ASCE)0733-9445(2008)134:8(1334).

[34] J.B. Mander, C.-T. Cheng, Seismic resistance of bridge piers based on damage avoidance design. Technical Report NCEER-97-0014, Buffalo, NY, USA, 1997.

[35] G. Vasdravellis, T.L. Karavasilis, B. Uy, Design rules, experimental evaluation, and fracture models for high-strength and stainless-steel hourglass shape energy dissipation devices, J. Struct. Eng. 140 (2014) 4014087. doi:10.1061/(ASCE)ST.1943-541X.0001014.

[36] C.B. Barthes, Design of Earthquake Resistant Bridges Using Rocking Columns, University of California, Berkeley, 2012. http://escholarship.org/uc/item/7gf04022.

[37] BS EN 1993-1-1, Eurocode 3: Design of steel structures - Part 1-1: General rules and rules for steel buildings, United Kingdom, 2009.

[38] BS EN 1993-1-5, Eurocode 3: Design of steel structures – Part 1-5: Plated structural elements, 2006.

[39] SCI/BCSA Connections Group, Joints in Steel Construction: Moment connections (P207), Imperial College London, Silwood Park Campus, Buckhurst Rd, Ascot SL5 7QN, United Kingdom, 1997.

[40] SCI/BCSA Connections Group, Joints in steel construction: Moment-resisting joints to Eurocode 3 (P398), Imperial College London, Silwood Park Campus, Buckhurst Rd, Ascot SL5 7QN, United Kingdom, 2013.

[41] H. Chi, J. Liu, M. Garlock, Design and Analytical Validation of Post-Tensioned Column Bases, in: Struct. Congr. 2008 Crossing Borders, April 24-26, American Society of Civil Engineers, Reston, Vancouver, British Columbia, Canada, 2008: pp. 1–6. doi:10.1061/41016(314)254.

[42] M.E.M. Garlock, R. Sause, J.M. Ricles, Behavior and Design of Posttensioned Steel Frame Systems, J. Struct. Eng. 133 (2007) 389–99. doi:10.1061/(ASCE)0733-9445(2007)133:3(389).

[43] H.-J. Kim, C. Christopoulos, Friction Damped Posttensioned Self-Centering Steel Moment-Resisting Frames, J. Struct. Eng. 134 (2008) 1768–1779. doi:10.1061/(ASCE)0733-9445(2008)134:11(1768).

[44] A.S. Tzimas, A.I. Dimopoulos, T.L. Karavasilis, EC8-based seismic design and assessment of self-centering steel frames with viscous dampers, J. Constr. Steel Res. 105 (2015) 60–73.

[45] G. Vasdravellis, T.L. Karavasilis, B. Uy, Finite element models and cyclic behavior of self-centering steel post-tensioned connections with web hourglass pins, Eng. Struct. 52 (2013) 1–16. doi:http://dx.doi.org/10.1016/j.engstruct.2013.02.005.

[46] A.I. Dimopoulos, T.L. Karavasilis, G. Vasdravellis, B. Uy, Seismic design, modelling and assessment of self-centering steel frames using post-tensioned connections with web hourglass shape pins, Bull. Earthq. Eng. 11 (2013) 1797–1816. doi:10.1007/s10518-013-9437-4.

[47] VSL International Ltd, Post-tensioning, stay cables & construction methods, Prod. Broch. VSL STRAND POST-TENSIONING Syst. (2013). www.vsl.com.

[48] D.G. Lignos, H. Krawinkler, Deterioration Modeling of Steel Components in Support of Collapse Prediction of Steel Moment Frames under Earthquake Loading, J. Struct. Eng.

137 (2011) 1291–1302. doi:10.1061/(ASCE)ST.1943-541X.0000376.

[49] FEMA, Quantification of building seismic performance factors (ATC-63 Project), USA, 2009.